Spectroscopy of NGC 4258 Globular Cluster Candidates: Membership Confirmation and Kinematics

Rosa A. González-Lópezlira[1] , Y. D. Mayya[2] , Laurent Loinard[1,3] , Karla Álamo-Martínez[4], George Heald[5],
Iskren Y. Georgiev[6], Yasna Órdenes-Briceño[7] , Ariane Lançon[8], Maritza A. Lara-López[9], Luis Lomelí-Núñez[2],
Gustavo Bruzual[1] , and Thomas H. Puzia[7]
[1] Instituto de Radioastronomía y Astrofísica, UNAM, Campus Morelia, Michoacan, C.P. 58089, Mexico; r.gonzalez@irya.unam.mx
[2] Instituto Nacional de Astrofísica, Óptica y Electrónica, Luis Enrique Erro 1, Tonantzintla, Puebla, C.P. 72840, Mexico
[3] Instituto de Astronomía, Universidad Nacional Autonoma de Mexico, Apartado Postal 70-264, 04510 Ciudad de Mexico, Mexico
[4] Departamento de Astronomia, Instituto de Física da Universidade Federal do Rio Grande do Sul, Brazil
[5] CSIRO Astronomy and Space Science, P.O. Box 1130, Bentley WA 6102, Australia
[6] Max-Planck Institut für Astronomie, Königstuhl 17, D-69117 Heidelberg, Germany
[7] Instituto de Astrofísica, Pontificia Universidad Católica de Chile, Av. Vicuña Mackenna 4860, 7820436 Macul, Santiago, Chile
[8] Observatoire Astronomique de Strasbourg, Université de Strasbourg, CNRS, UMR 7550, 11 rue de l'Université, F-67000 Strasbourg, France
[9] Dark Cosmology Centre, Niels Bohr Institute, University of Copenhagen, Juliane Maries Vej 30, DK-2100 Copenhagen, Denmark
Received 2018 November 16; revised 2019 February 19; accepted 2019 March 15; published 2019 May 1

Abstract

We present multiobject spectroscopic observations of 23 globular cluster candidates (GCCs) in the prototypical megamaser galaxy NGC 4258, carried out with the Optical System for Imaging and low-Intermediate-Resolution Integrated Spectroscopy instrument at the 10.4 m Gran Telescopio Canarias. The candidates have been selected based on the $(u^* - i')$ versus $(i' - K_s)$ diagram, in the first application of the $u^*i'K_s$ method to a spiral galaxy. In the spectroscopy presented here, 70% of the candidates are confirmed as globular clusters (GCs). Our results validate the efficiency of the $u^*i'K_s$ method in the sparser GC systems of spirals, and given the downward correction to the total number of GCs, the agreement of the galaxy with the correlations between black hole mass and the total number and mass of GCs is actually improved. We find that the GCs, mostly metal-poor, corotate with the H I disk, even at large galactocentric distances.

Key words: galaxies: evolution – galaxies: formation – galaxies: kinematics and dynamics – galaxies: spiral – galaxies: star clusters: general – globular clusters: general

1. Introduction

It has become commonplace to state that globular clusters (GCs) are powerful signposts of the structure, dynamics, and star formation and assemblage histories of their host galaxies. Not only are they compact and bright, and hence traceable to large distances, but they do correlate with global properties and other components of their hosts, such as their luminosity (e.g., Peng et al. 2008; Georgiev et al. 2010), light concentration and stellar velocity dispersion (Harris et al. 2013), total stellar mass and bulge light (Rhode 2012), and total halo (Spitler & Forbes 2009; Harris et al. 2017) and central supermassive black hole masses (e.g., Burkert & Tremaine 2010; Harris & Harris 2011; Sadoun & Colin 2012; Harris et al. 2014). However, until now, studies of GC systems have focused on early-type galaxies, given their significantly larger number of GCs and the ease of their identification in the absence of a dusty stellar disk, composed of partially resolved, bright sources.

Although understandable given the obvious difficulties, the scarcity of studies of late-type galaxies constitutes a real obstacle to actually using GC systems as probes of galaxy formation and evolution, for several reasons, as expressed already a couple of decades ago (e.g., Kissler-Patig et al. 1999). First, we do not really know how typical the GC system of our Galaxy is, and yet it is the standard to which all other systems are compared. More importantly, perhaps, while there seems to be a consensus that elliptical galaxies, and hence their GC systems, form through mergers, there is now mounting observational (e.g., Förster Schreiber et al. 2009; Tacconi et al. 2013; Dessauges-Zavadsky et al. 2015; Patrício et al. 2018) and

theoretical (e.g., Dekel et al. 2009; Kruijssen 2015) evidence that massive stellar clusters form at $z \geqslant 2$ by the fragmentation of gaseous disks, rotating but turbulent, suffering intense, cold gas accretion flows. GCs would be the relics of this star formation epoch, and low-mass spirals may still contain relatively undisturbed primeval systems, given their slightly lower major $(M_{sat}/M_{primary} \geqslant 1:4)$ merger rates (Rodriguez-Gomez et al. 2015).

Motivated originally to explore the correlation between total number of GCs, N_{GC}, and central black hole mass, $M_\bullet$ (e.g., Burkert & Tremaine 2010; Harris & Harris 2011) in spiral galaxies, we have embarked on a campaign to observe nine northern galaxies closer than 16 Mpc, with good measurements of their central black hole masses. The first analyzed target was the megamaser prototype NGC 4258 (M106). It is the largest member of the Canes II group, populated mostly by late-type spirals and irregular galaxies. Thanks to a circumnuclear maser disk, NGC 4258 has the most precise extragalactic $M_\bullet$ measurement. It also follows several correlations established for elliptical galaxies, like those between $M_\bullet$ and bulge luminosity and mass (Läsker et al. 2016).

Using the $u^*i'K_s$ photometric method (Muñoz et al. 2014), described in Section 2, González-Lópezlira et al. (2017) selected a sample of GC candidates (GCCs) in NGC 4258 and determined that it likewise falls on the N_{GC} versus $M_\bullet$ correlation. Interestingly, the projected spatial distribution of the González-Lópezlira et al. clusters appears disky and aligned with the galaxy, although their colors rule out that they are young clusters in the stellar disk (see González-Lópezlira et al. 2017 and Section 2). The $u^*i'K_s$ approach is possibly the most

Table 1
Summary of Photometric Observations

Filter	λ_{cen}[a]	FWHM[b]	Exposure (s)	Depth AB mag	m_0^{TO} AB mag
u^*	3793 Å	654 Å	13360	26.0	23.1
g'	4872 Å	1434 Å	10400	26.5	22.2
r'	6276 Å	1219 Å	3500	25.4	21.7
i'	7615 Å	1571 Å	8080	25.7	21.5
K_s	2.15 μm	0.33 μm	200	21.5	21.3

Notes.
[a] The central wavelength between the two points defining FWHM (http://svo2.cab.inta-csic.es/svo/theory/fps3/index.php?id=CFHT/).
[b] *Ibid.*

efficient photometric method of selecting GCCs in elliptical galaxies. This paper analyzes spectra of the GCC sample of NGC 4258, with two main goals: quantify the efficiency of the $u^*i'K_s$ method for the study of the much sparser GC systems of spirals, and investigate the kinematics of the NGC 4258 GCs. The paper is organized as follows. Section 2 recapitulates the sample selection process carried out in González-Lópezlira et al. (2017). Section 3 presents the spectroscopic observations, their reduction, and the determination of the line-of-sight velocities of the candidates. In Section 4 we derive the kinematics of the system; the metallicity of the composite spectra of the whole sample is estimated in Section 5; the efficiency of the $u^*i'K_s$ method is analyzed in Section 6. Finally, the discussion and conclusions are presented in Section 7.

2. GCC Sample

González-Lópezlira et al. (2017) defined a sample of 39 GCCs in NGC 4258, from Canada–France–Hawaii Telescope (CFHT) optical (u^*, g', r', i') and near-infrared (K_s) data, both archival and proprietary. Potential candidates had photometric errors smaller than 0.2 mag in the i' band and were within ±3.6 mag of the expected GC luminosity function turnover (LFTO) magnitude in every filter. Also, they were neither saturated nor blended or close to bright neighbors. These latter requirements against crowding eliminated all sources within an elliptical region centered on NGC 4258, with semimajor axis = 3′.5, or 0.37 R_{25}, axis ratio = cos(67°), and the same position angle (P.A.) as the galaxy, of 150° (de Vaucouleurs et al. 1991). Table 1 gives a summary of the photometric observations, including exposure times, depths, and expected location of the LFTO. Given the significantly shorter exposure time, all of the analysis by González-Lópezlira et al. was limited by the K_s-band image; the GC luminosity function was complete to ∼20.5 AB mag in this wavelength (González-Lópezlira et al. 2017).

Our main selection tool was the ($u^* - i'$) versus ($i' - K_s$) color–color diagram (Muñoz et al. 2014); this was the first application of the $u^*i'K_s$ technique to a spiral galaxy. The GCC selection region in this diagram was determined from the area that contains the highest density (more than 2000) of spectroscopically confirmed GCs in M87 (Muñoz et al. 2014; Powalka et al. 2016). The region has approximately the shape of a drop or pennon and appears drawn in brown in Figure 1. Crucially, it is well separated from the loci occupied by background galaxies, foreground Galactic stars, and young stellar clusters in the disk of spiral galaxies. To further decrease the probability of contamination by background galaxies, as well as by dwarf galaxies in NGC 4258
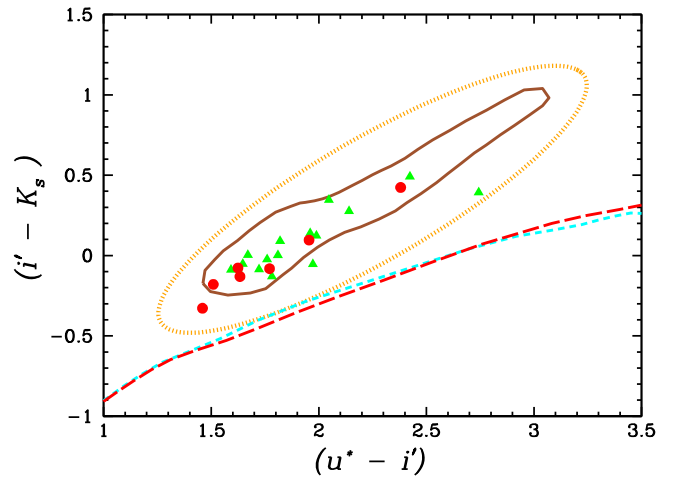
Figure 1. $u^*i'K_s$ color–color diagram. The dotted orange line delimits the region occupied by BC03 single stellar populations with ages 8–12 Gyr and metallicities $0.0004 \leqslant Z \leqslant 0.05$; the solid brown contour traces the area with the highest density of spectroscopically confirmed GCs in M87; the short-dashed cyan and long-dashed red lines are zero-age main sequences with $Z = 0.008$ and $Z = 0.02$, respectively, and sketch the loci of stars in the Milky Way. Green triangles: spectroscopically confirmed GCCs; red circles: GCCs rejected by spectroscopic observations (see the text, Section 3.2).

itself, only sources with i'-band FWHM $\leqslant 0''.84$ (31 pc at 7.6 Mpc, the distance to NGC 4258; Humphreys et al. 2013) and SExtractor (Bertin & Arnouts 1996) light-concentration parameter SPREAD_MODEL $\leqslant 0.017$ were kept.[10] Half-light radii of the objects, measured by fitting King profiles to their radial light distributions with the program ISHAPE (Larsen 1999), were all smaller than 6 pc.

A couple of GCCs in the spectroscopic sample come from a previous, unpublished photometric sample of 38 objects (the published and unpublished samples share 30 sources in common). In this case, the selection region in the $u^*i'K_s$ diagram was the ellipse centered at ($u^* - i'$) = 2.25, ($i' - K_s$) = 0.35, with semimajor and semiminor axes 1.25 mag and 0.345 mag, respectively, and rotated 39° counterclockwise from the ($u^* - i'$) axis. This elliptical region contains the pennon, was delimited based on Bruzual & Charlot (2003, hereafter BC03) model single stellar populations (SSPs), and is drawn with a dotted orange line in Figure 1. The figure also shows two lines, short-dashed cyan and long-dashed red, that represent zero-age main sequences with, respectively, $Z = 0.008$ and $Z = 0.02$. They trace a band of Galactic field stars that brushes the orange ellipse near ($u^* - i'$) ∼ 1.8, ($i' - K_s$) ∼ −0.4. In view of potential contamination from these objects, the unpublished sample also had minimum size bounds in the i' filter (FWHM = $0''.65$, SPREAD_MODEL = 0.002). These minimum size bounds, however, would have eliminated GCs with $r_e < 4.7$ pc, or about half the total in the Milky Way (MW).

GCCs in either of the photometric samples are identified with the acronym GLL ("Globular Luis Lomelí") before their equinox J2000.0 equatorial coordinates. The spectroscopic sample, enumerated in Table 2, includes GLL GCCs, objects in either of the color–color selection regions that did not fulfill the light concentration requirements, and random objects in the

---

[10] The SPREAD_MODEL value for each object results from the comparison between its best fitting point-spread function (PSF) and the convolution of such PSF with an exponential disk with scale length FWHM$_{PSF}$/16, where FWHM$_{PSF}$ is the full width at half maximum of the same PSF (Desai et al. 2012).

Table 2
Target Velocity Fit Parameters, *Hubble Space Telescope* Image Information, and Probable Object Types

Name	R.A. J2000 (deg)	Decl. J2000 (deg)	S/N	$V_{\rm proj}$ (km s^{-1})	$\Delta V_{\rm proj}$ (km s^{-1})	r Value	Template	Range (Å)	$V_{\rm H\,I,proj}$ (km s^{-1})	$\Delta V_{\rm H\,I,proj}$ (km s^{-1})	*HST* Image	FWHM (″)	FWHM PSF (″)	Object Type
							Confirmed GC candidates							
GLL J121851 +471400	184.7166	47.2335	28	324.0	72.6	4.92	fglotemp	4400–7100	378.5	14.9	hst_11570_97_acs_wfc_f555w	0.160	0.100	GC
GLL J121852 +472201	184.7205	47.3672	11	779.4	82.3	2.58	fglotemp	4100–7198	573.4	36.8	hst_11570_86_acs_wfc_f555w	0.130	0.105	GC
GLL J121854 +472318	184.7266	47.3885	31	496.9	57.4	5.35	fglotemp	4100–7198	555.1	23.1	hst_11570_91_acs_wfc_f555w	0.195	0.100	GC
GLL J121856 +471411	184.7345	47.2366	12	315.9	51.7	3.67	fs2temp	4000–7198	364.0	21.1	hst_11570_97_acs_wfc_f555w	0.165	0.105	GC
GLL J121857 +472330	184.7384	47.3918	23	338.7	48.3	8.78	fglotemp	4100–7198	528.2	8.7	hst_11570_91_acs_wfc_f555w	0.155	0.105	GC
GLL J121859 +472107	184.7500	47.3520	52	662.2	69.6	6.00	fglotemp	3720–7100	514.3	25.8	hst_11570_86_acs_wfc_f555w	0.150	0.100	GC
J121901+471859[a]	184.7553	47.3166	9	577.3	49.4	4.31	fs2temp	4000–7000	449.5	44.3	hst_11570_88_acs_wfc_f555w	0.105	0.100	GC
GLL J121901 +471905	184.7565	47.3183	15	260.1	68.7	3.71	fglotemp	4100–7000	448.4	43.8	hst_11570_88_acs_wfc_f555w	0.155	0.095	GC
GLL J121902 +472048	184.7585	47.3469	33	383.8	52.4	5.44	fglotemp	4000–6950	488.6	22.9	hst_11570_86_acs_wfc_f555w	0.175	0.095	GC
GLL J121902 +472125	184.7622	47.3572	23	608.3	23.6	9.82	fglotemp	4000–6850	488.8	11.8	hst_11570_99_acs_wfc_f555w	0.125	0.090	GC
GLL J121902 +472043	184.7624	47.3453	35	625.8	31.4	7.78	fglotemp	4000–6850	477.0	9.0	hst_11570_88_acs_wfc_f555w	0.155	0.100	GC
GLL J121908 +471355	184.7847	47.2322	27	257.9	47.5	5.86	fglotemp	4000–7400	322.2	31.3	hst_11570_96_acs_wfc_f555w	0.140	0.100	GC
GLL J121925 +471228	184.8578	47.2079	36	282.0	39.0	7.03	fglotemp	4200–7198	289.0	14.2	hst_11570_94_acs_wfc_f555w	0.165	0.100	GC
GLL J121928 +471152[b]	184.8685	47.1978	17	505.5	72.8	4.19	fglotemp	4300–7198	290.8	14.2	hst_11570_94_acs_wfc_f555w	0.200	0.100	GC
GLL J121929 +471215	184.8711	47.2042	54	219.5	17.1	14.02	fglotemp	4250–7198	298.9	16.3	hst_11570_94_acs_wfc_f555w	0.150	0.100	GC
GLL J121934 +471316	184.8944	47.2212	21	401.2	66.6	4.03	fglotemp	3720–7198	344.7	6.0	hst_10399_50_acs_wfc_f606w	0.170	0.080	GC
							Rejected GC candidates							
GLL J121852 +471313	184.7187	47.2204	12	−209.3	47.9	5.66	eltemp	4100–7198	368.1	15.3	hst_11570_97_acs_wfc_f555w	0.105	0.100	star
GLL J121854 +472144[c]	184.7261	47.3625	8	543.6	53.7	4.69	fm32temp	4100–7198	564.3	32.6	hst_11570_90_acs_wfc_f555w	0.155	0.090	dwarf gal/GC
GLL J121854 +472245	184.7278	47.3792	53	−199.3	14.6	18.59	fm32temp	4000–7100	558.8	25.4	hst_11570_91_acs_wfc_f555w	0.095	0.10	star
GLL J121903 +472613[b]	184.7654	47.4372	20	470.2	158.1	1.64	fglotemp	4300–5500[d]	512.6	7.7	no images			dwarf gal/GC
GLL J121905 +472422	184.7744	47.4063	86	750.7	49.7	5.42	fm32temp	4100–6600	498.4	6.1	hst_11570_91_acs_wfc_f555w	0.285	0.100	dwarf gal/GC
GLL J121909 +471335	184.7909	47.2265	12	400.3	101.4	2.43	eltemp	4300–5500[e]	309.4	34.5	hst_11570_96_acs_wfc_f555w	0.160	0.100	dwarf gal/GC

Table 2
(Continued)

Name	R.A. J2000 (deg)	Decl. J2000 (deg)	S/N	V_{proj} (km s^{-1})	ΔV_{proj} (km s^{-1})	r Value	Template	Range (Å)	$V_{H\,l,proj}$ (km s^{-1})	$\Delta V_{H\,l,proj}$ (km s^{-1})	HST Image	FWHM (″)	FWHM PSF (″)	Object Type
GLL J121910 +471343	184.7931	47.2287	23	172.2	104.9	4.34	fglotemp	4000–7200	308.9	37.1	hst_11570_96_acs_wfc_f555w	0.250	0.100	dwarf gal/GC
Confirmed noncandidates														
J121853+472136	184.7219	47.3600	21	853.5	36.2	8.05	fn7331temp	4100–7198	578.3	45.7	hst_11570_90_acs_wfc_f555w	0.235	0.100	dwarf gal (?)
J121907+472113	184.7795	47.3538	19	43004.9	31.1	7.90	eltemp	4000–6500	472.4	15.6	hst_11570_99_acs_wfc_f555w	0.240	0.090	gal
J121924+471306	184.8518	47.2185	12	12576.2	19.8	5.66	femtemp97	4100–7198	300.1	12.6	hst_11570_94_acs_wfc_f555w	0.115	0.100	gal
J121849+471357	184.7042	47.2325	2	38418.3	46.6	3.26	femtemp97	3720–7198	386.2	14.6	hst_11570_97_acs_wfc_f555w	0.100	0.100	gal (?)
J121853+471330	184.7232	47.2250	19	329.3	16.4	10.32	femtemp97	3720–7198	366.4	16.2	hst_11570_97_acs_wfc_f555w	0.117	0.100	H II reg
J121854+472235	184.725	47.3764	24	618.8	13.9	12.74	femtemp97	3720–7198	564.4	25.3	hst_11570_91_acs_wfc_f555w	0.100	0.100	H II reg
J121854+471324	184.7284	47.2235	18	10015.5	99.5	2.67	eltemp	4100–7198	363.2	17.0	hst_11570_97_acs_wfc_f555w	0.115	0.100	gal
J121856+471342	184.7374	47.2286	12	380.4	16.0	10.70	femtemp97	3720–7198	356.8	20.8	hst_11570_90_acs_wfc_f555w	0.120	0.090	H II reg
J121920+471332	184.8365	47.2256	12	104927[f]					302.8	12.2	hst_11570_94_acs_wfc_f555w	0.310	0.100	gal
J121930+471254	184.8786	47.2152	3	43234.8	51.8	2.17	femtemp97	4000–7198	321.3	11.1	hst_11570_94_acs_wfc_f555w	0.267	0.100	gal (?)

Notes.

[a] Rejected from unpublished sample due to small size, and from published (González-Lópezlira et al. 2017) sample because of its colors (see the text).

[b] In unpublished sample, then rejected from published sample because of its colors.

[c] Should not have been in sample, owing to axis ratio <0.7.

[d] With full spectral range (4000–6800 Å), best correlation (r value 2.04) found for template sptemp, with $V_{proj} = 18461 \pm 85$ km s^{-1}. However, spectral lines are consistent with an old stellar population at the systemic velocity of NGC 4258 (Figure 17).

[e] With full spectral range (4000–7400 Å), best correlation (r value 2.86) found for template sptemp, with $V_{proj} = 12141 \pm 79$ km s^{-1}. However, spectral lines are consistent with a stellar population at the systemic velocity of NGC 4258 (Figure 17).

[f] No available *rvsao* template fits the very obvious emission lines. The highest r value is 3.29 for sptemp, with $V_{proj} = 1071 \pm 54$ km s^{-1}. fn7331temp comes closest to the real measurement; it yields $z = 0.31$, with $r = 0$.
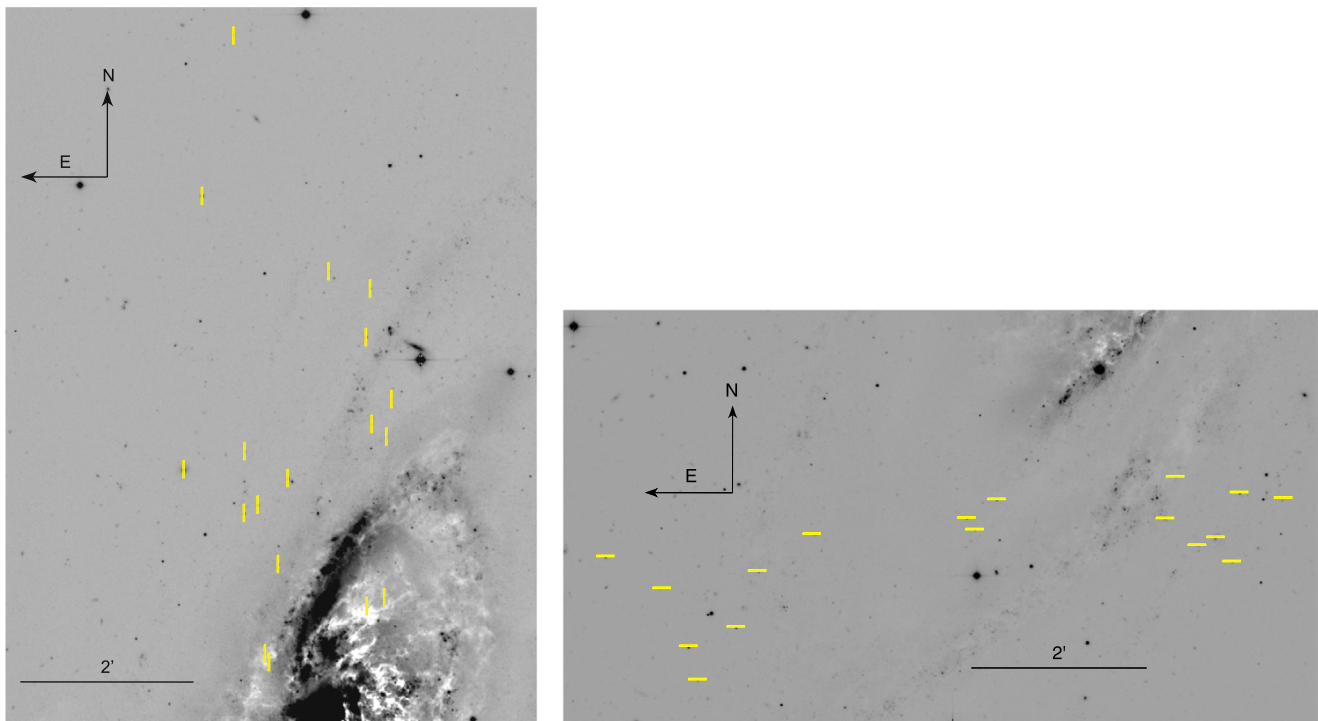
Figure 2. Sections of archival CFHT r'-band image of NGC 4258 showing, in yellow, the location of slitlets observed with GTC/OSIRIS. Left: field NS1, centered at R.A. = $12^{\rm h}18^{\rm m}52\overset{s}{.}10$, decl. = $+47°19'51\overset{''}{.}8$ (J2000.0); right: field EW4, centered at R.A. = $12^{\rm h}19^{\rm m}27\overset{s}{.}17$, decl. = $+47°13'16\overset{''}{.}4$ (J2000.0).

observed fields as additional controls. The two latter classes of objects are listed by their equinox J2000.0 equatorial coordinates, with no preceding acronym.

3. Spectroscopic Observations

The data set used in this work was obtained with the Optical System for Imaging and low-Intermediate-Resolution Integrated Spectroscopy (OSIRIS), in multi-object spectroscopy (MOS) mode, at the Nasmyth-B focus of the Gran Telescopio Canarias (GTC).[11] OSIRIS has two mosaicked Marconi CCD44-82 detectors, with a $9\overset{''}{.}4$ gap between them. Each detector has 2048×4096 pixels, whose physical size is $15\,\mu$m on a side, for a scale of $0\overset{''}{.}127$ on the sky. In standard observing modes, however, pixels are binned 2×2, for an effective spatial scale of $0\overset{''}{.}254$. We observed with the R1000B grism, whose wavelength range goes from $\sim$3700 to 7500 Å. The slit width of $1''$ yielded a resolution of 5.51 Å. OSIRIS offers a maximum field of view (FOV) of $7\overset{'}{.}5 \times 6\overset{'}{.}0$ for slitlet placement. However, we used only an FOV of $7\overset{'}{.}5 \times 3\overset{'}{.}0$ in each of our two pointings in order to ensure the coverage of the complete spectral range of 3700–7500 Å for all observed targets.

The data set consists of spectra in two fields, located north (NS1) and south (EW4) of the minor axis of NGC 4258. The NS1 field was oriented N–S, with the dispersion axis running E–W; conversely, the EW4 field was oriented E–W, with the dispersion axis along the N–S direction. Their centers were, respectively, R.A. = $12^{\rm h}18^{\rm m}52\overset{s}{.}10$, decl. = $+47°19'51\overset{''}{.}8$, (J2000.0) for field NS1, and R.A. = $12^{\rm h}19^{\rm m}27\overset{s}{.}17$, decl. = $+47°13'16\overset{''}{.}4$ (J2000.0) for field EW4.

Spectra were obtained for slightly over 50% of the GCC sample defined by González-Lópezlira et al. (2017). The positions of the science slits in each field are shown as yellow boxes, over grayscales of the CFHT r' image of the galaxy, in Figure 2. For illustration purposes, all slits have been drawn with the same size; in actuality, slitlets had varying lengths, so as to not overlap, and included object-free regions to allow for the subtraction of sky spectra. Observations of reference stars for astrometry were also carried out (positions not shown).

Each field was observed for a total of 3975 s, divided into three exposures of 1325 s to facilitate cosmic-ray cleaning. Standard stars, arc lamps, bias, and flat-field frames were also obtained for each pointing. Field NS1 was secured on 2017 May 24, a clear, dark night; field EW4 was observed during 2017 May 30 and 31, which were gray nights with some cloud cover. Consequently, while the average signal-to-noise ratio (S/N) of the sources in field NS1 is $\sim$29, for those in field EW4 it is only $\sim$19, as gauged by the routine DER_SNR.[12] A summary of the spectroscopic observations is given in Table 3.

3.1. Data Reduction

The reduction of the spectroscopic data was performed with *GTCMOS*,[13] an ad hoc pipeline based on IRAF[14] (Tody 1986, 1993) tasks. The reduction procedure has been described at length by Gómez-González et al. (2016), but we give a brief summary here.

---

[11] Gran Telescopio Canarias is a Spanish initiative with the participation of Mexico and the University of Florida, USA, and is installed at the Roque de los Muchachos Observatory in the island of La Palma. This work is based on the proposal GTC17-9AMEX, using Mexican share of the GTC time.

[12] Stoehr, F., ST-ECF Newsletter, Issue 42, www.stecf.org/software/ASTROsoft/DER_SNR/.

[13] http://www.inaoep.mx/~ydm/gtcmos/gtcmos.html

[14] IRAF is distributed by the National Optical Astronomy Observatories, which are operated by the Association of Universities for Research in Astronomy, Inc., under cooperative agreement with the National Science Foundation.

Table 3
Observation Log

Run/Field	Principal Investigator	Date	Position Angle (deg)	Slit Width ($''$)	Grism	Exp. Time (s)	Air Mass	Seeing ($''$)	Night	Standard Star
2017A-NS1	R. González-Lópezlira	2017 May 24	270	1.0	R1000B	3×1325	1.42	0$\farcs$7	Dark, clear	Ross 640
2017A-EW4	R. González-Lópezlira	2017 May 30	0	1.0	R1000B	2×1325	1.24	0$\farcs$8	Gray, clouds	GD153
2017A-EW4	R. González-Lópezlira	2017 May 31	0	1.0	R1000B	1325	1.39	0$\farcs$8	Gray, clouds	GD153
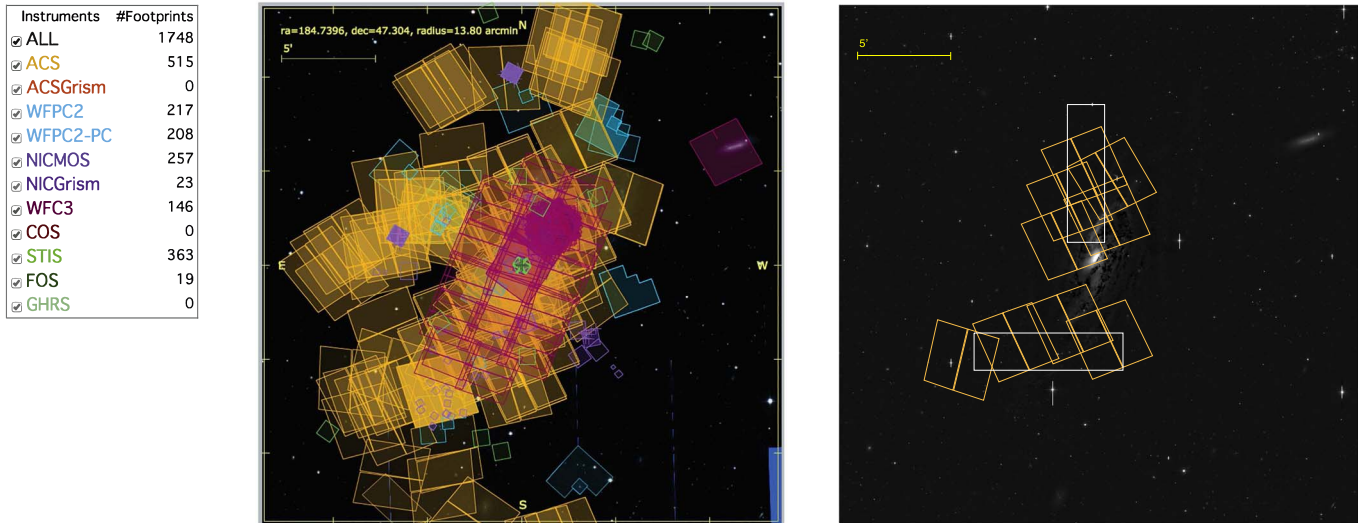
Figure 3. *HST* footprints of NGC 4258 data. Left: all available Hubble Legacy Archive data, superimposed on a Digitized Sky Survey image. The footprints for each instrument are coded by color; the legend indicates the number of images obtained by each camera or spectrograph. The data are so plentiful that the galaxy is not visible under the footprints. Right: footprints of ACS frames used in this work (golden yellow), superimposed on the CFHT i'-band data of the galaxy; the outlines of the fields observed with the GTC are shown in white. The physical and display scales in both panels have been roughly matched.

The pipeline tiles the two OSIRIS CCDs and corrects for geometrical distortions. All tiled bias frames in an observing block are combined into a master bias image with a median algorithm; the master bias is then subtracted from all of the images in the block. All images of each target are then combined, also with a median algorithm, a procedure that cleans cosmic rays from the final frames. Arc spectra are also tiled and combined into a single arc image, which is used for wavelength calibration. The pipeline also corrects the curvature of the slit images in the spatial direction and obtains independent dispersion solutions for each slitlet, using a spline3 function of order 2. Final rms errors are better than $0.5\,\text{Å}$. The best solution for each slitlet is used to create a wavelength-calibrated 2D image, with the spectral axis linearly resampled to a dispersion of $2.1\,\text{Å pixel}^{-1}$. The dispersion-corrected spectra are also shifted linearly, in order to force the centroid of the [O I]$\lambda 5577$ sky line in every spectrum to lie at its rest wavelength.

Standard star spectra are reduced individually in a similar fashion. Once spectra are extracted, sensitivity tables between the flux and count rate at all available spectral bands are obtained with the IRAF task *standard*. Atmospheric extinction corrections are performed, for both standard stars and targets, by combining the extinction curve for the observatory with the registered air masses of the observations.

The IRAF task *apall* was used for the extraction of the spectra of individual targets from the wavelength- and flux-calibrated 2D images. The background (sky plus underlying galaxy) spectrum was also subtracted during the extraction procedure. For all of the targets, the continuum is well registered so as to enable in situ tracing. The width of the extraction window is kept between 4 and 6 pixels (1–1″5), which has been found to maximize the S/N of the extracted spectrum. Most of the slitlets were long enough to include object-free pixels for the extraction of the background spectrum. In a few cases, where this was not possible, background zones were selected from slitlets that were spatially closest to the object.

The sky plus underlying galaxy background is as bright as or, very often, brighter than the object within the extraction window. Furthermore, sky noise increases monotonically toward the blue, that is, almost by a factor of two between 5000 and $4000\,\text{Å}$. Thus, the S/N of the extracted spectrum, especially blueward of $5000\,\text{Å}$, is mainly governed by the photon noise of the background spectrum. We considered only those parts of each spectrum where the S/N pixel^{-1} (of $2.1\,\text{Å}$ width) is above at least 10. In Table 2 we give the S/N, again as estimated by the routine DER_SNR, as well as the useful wavelength range for each spectrum.

3.2. Line-of-sight Velocities

Projected heliocentric velocities of the GCCs and other targets were determined with the Fourier cross-correlation method implemented in the *xcsao* task of the *rvsao* package (Kurtz & Mink 1998) within IRAF. For comparison with our spectra, we used some of the templates provided by the Smithsonian Astrophysical Observatory (SAO; http://tdc-www.harvard.edu/software/rvsao/Templates/). We employed the two templates derived from M31 GCs (called *fglotemp* and *fs2temp*); a synthetic galaxy emission line spectrum (*femtemp97*) that provides a good match to H II regions; and four galaxy templates: a composite spiral galaxy template, a composite elliptical galaxy template, one derived from M32, and one produced from NGC 7331 (respectively, *sptemp, eltemp, fm32temp, fn7331temp*). All templates were resampled to the resolution of the spectra obtained with OSIRIS/GTC and reduced with *GTCMOS*. The goodness of fit is gauged through the r value, also provided by the *xcsao* task for each comparison; the higher the r value, the better the fit. The sky region, between 5500 and $5650\,\text{Å}$, was always excluded from the fits, as were the edges of the spectra in the cases where they looked noisy.

For an object to be considered a GC, the highest r value should occur for the M31 GC templates in the whole observed spectral window, and the derived heliocentric velocity had to lie in the expected range of objects in NGC 4258, between $\sim$300 and $\sim$750 km s^{-1}. Objects that had a good match in the
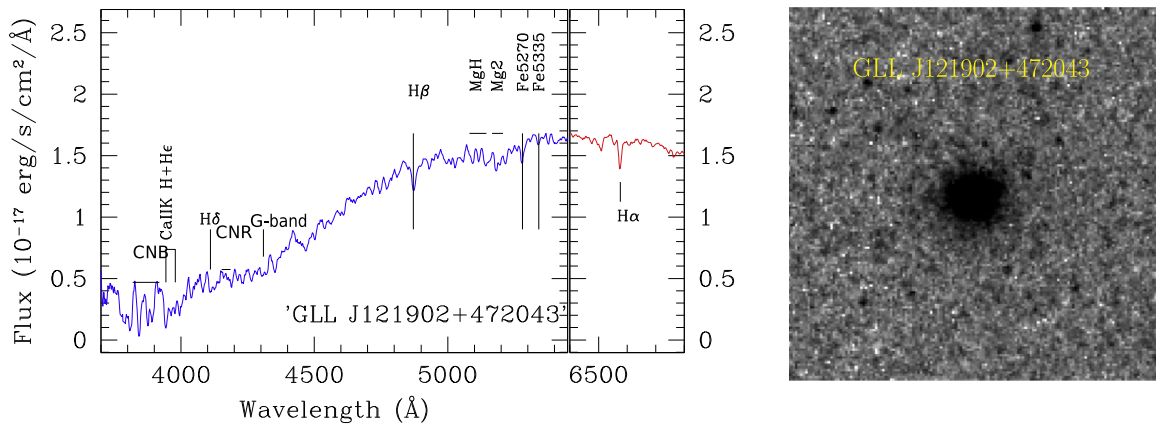
Figure 4. OSIRIS spectrum (left) and *HST* grayscale (right) of confirmed GC candidate GLL J121902+472043.

same velocity range with the template femtemp97 are likely H II regions. All other objects were considered either as foreground stars (velocity less than the minimum allowed and FWHM similar to the PSF FWHM; see Table 2, columns 13 and 14), dwarf satellite galaxies (velocity in the range), or background galaxies (velocity larger than the maximum permitted).

The classification of all objects was further visually confirmed through the inspection of *Hubble Space Telescope* (*HST*) archival images, as NGC 4258 has one of the largest Hubble Legacy Archive (HLA)[15] data collections available (Figure 3, left panel[16]). All of the frames used in this work were acquired with the Advanced Camera for Surveys (ACS); their footprints are illustrated in golden yellow in the right panel of Figure 3, superimposed on the CFHT i'-band data of NGC 4258. Except in one case, the images were obtained through the F555W filter and proceed from proposal GO 11570 (P.I. A. Riess). For GLL J121934+471316, we used an F606W image from proposal GO 10399 (P.I. L.J. Greenhill); no *HST* image was found for GLL J121903+472613. Via this comparison with ACS data, for example, we assessed that GLL J121854+472245 is likely a star; we also rejected GLL J121910+471343, given its very elongated aspect, in spite of having a best match with a GC spectral template. Confirmed and rejected GCC candidates are shown as, respectively, green triangles and red circles in Figure 1. For each observed source, together with its name and J2000 coordinates, Table 2 lists its projected velocity V_{proj} and error ΔV_{proj}, the r value of the cross-correlation, the velocity template with the best fit, the spectral range over which the cross-correlation was performed, the projected velocity of the H I gas at the position of the source $V_{H I,proj}$ and its error $\Delta V_{H I,proj}$ (see Section 4), the archival *HST* image inspected, the FWHM of the object, the FWHM of the PSF of the image, and the probable object type. The table has three sections: confirmed candidates, rejected candidates, and confirmed noncandidates. Among the rejected candidates, given their spectra and projected velocities, GLL J121854+472144, GLL J121903+472613, GLL J121905+472422, GLL J121909+471335, and GLL J121910+471343 are consistent with being satellite dwarf galaxies of NGC 4258. The first three objects in the third section (confirmed

noncandidates) were within the elliptical selection region in the $u^*i'K_s$ diagram described in Section 2, that is, their colors resemble those of GCs. J121907+472113 had been discarded mainly on account of its angular size, and indeed it is a spiral galaxy at $z = 0.14$. J121924+471306 was blended in the CFHT data and has a small axis ratio (0.5); it appears to be a galaxy at $z = 0.04$, with emission lines in its spectrum. J121853+472136, however, although blended in the CFHT data and with a small axis ratio (0.6), could be associated with NGC 4258, given its spectrum and projected velocity. The remaining noncandidates were observed only as a consistency check because they fell on the two fields targeted with the GTC.

Figure 4 shows the OSIRIS spectrum in the observed wavelength and *HST* image of the confirmed candidate GLL J121902+472043. Spectra and images of the remaining confirmed candidates are displayed in Figure 16 in the Appendix. For most objects, the spectra are presented in two windows, one shortward of 5450 Å and one showing the Hα region. Spectra have been smoothed with a boxcar of size five pixels. The most characteristic spectral lines of old stellar populations or H II regions are indicated.[17]

Spectra and images of rejected candidate GLL J121852 +471313 and confirmed noncandidate J121856+471342 are presented, respectively, in Figures 5 and 6. Figures 17 and 18 in the Appendix comprise spectra and images of the rest of the rejected candidates and confirmed noncandidates, respectively.

4. Rotation and Velocity Dispersion

The projected spatial distribution of the GCC sample determined in González-Lópezlira et al. (2017, their Figure 10) suggests a disk. We can now investigate the kinematics of the system and whether there is evidence of rotation.

Figure 7 shows the projected line-of-sight (LOS) velocities of the confirmed GCCs versus their projected distances from the center of the galaxy; there is no correlation between these two parameters (correlation coefficient of −0.33). Figure 8, on the other hand, plots the highly probable GCCs (solid circles, confirmed GCCs in Table 2) on the NGC 4258 H I velocity field map from the Westerbork Synthesis Radio Telescope Hydrogen Accretion in LOcal GAlaxieS (HALOGAS) survey

---

15 https://hla.stsci.edu
16 The graphic was produced using the HLA site, with the footprints superimposed on a Digitized Sky Survey (http://archive.stsci.edu/dss/) image.

17 We note here that lines are not conspicuous in either GLL J121856+471411 or GLL J121901+471859; however, the S/Ns of their spectra are not high enough to confidently eliminate them from the list of confirmed candidates on this basis.
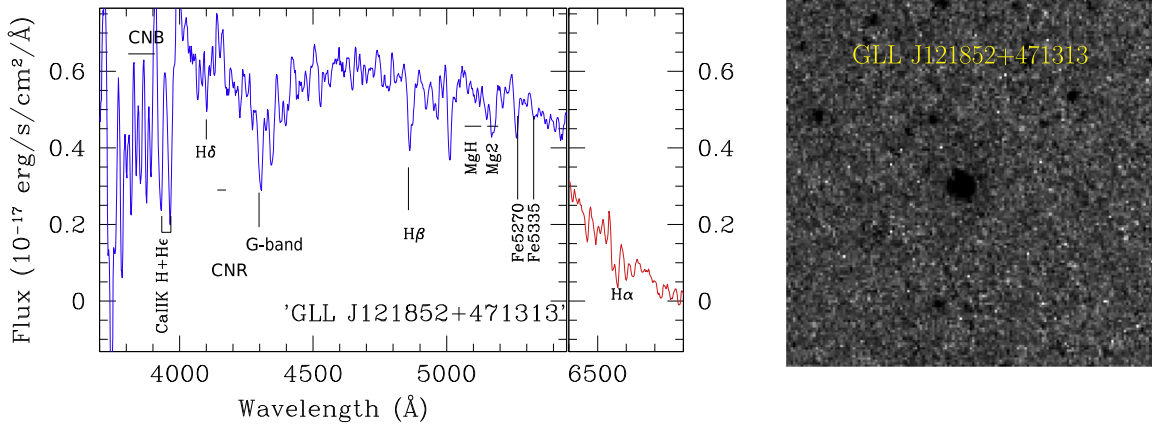
Figure 5. OSIRIS spectrum (left) and *HST* grayscale (right) of rejected GC candidate GLL J121852+471313. The spectrum correlates best with *eltemp*, a non-GC template, and has a negative radial velocity.
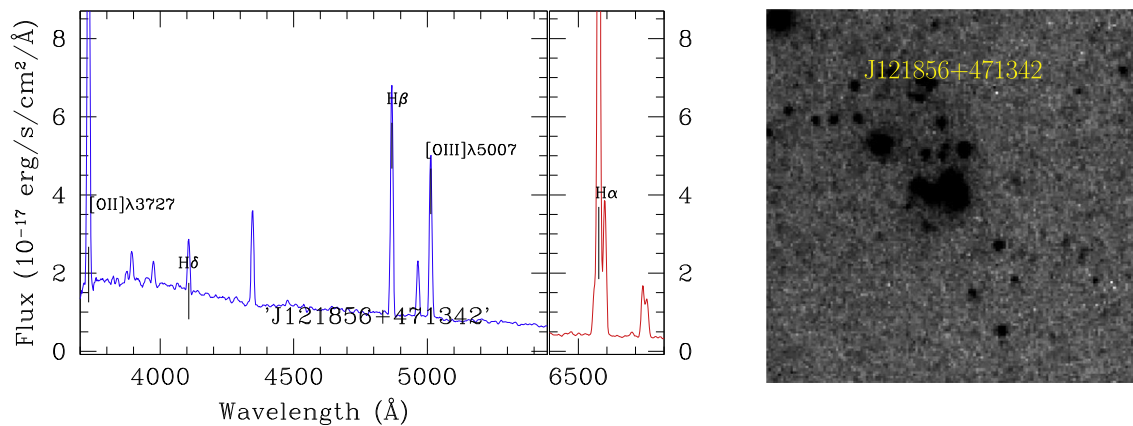
Figure 6. OSIRIS spectrum (left) and *HST* grayscale (right) of noncandidate J121856+471342.

(Heald et al. 2011). LOS velocity is coded by color, as indicated in the sidebar, and the same scale is used for both the H I and the GCCs. This graphic shows that the GCCs south of the rotation axis are approaching us, while most of the ones in the observed northern field are receding.

Finally, Figure 9 displays the measured LOS projected velocities versus azimuthal angle, measured counterclockwise from north, for the confirmed GCCs (solid green triangles), rejected candidates that could be satellite galaxies of NGC 4258 (solid red circles), rejected candidates that appear to be foreground stars (solid blue squares), and one noncandidate that could also be an object associated with NGC 4258 (open red circle). Our GTC objects are overplotted on the NGC 4258 projected H I gas heliocentric velocities (gray curve) in the elliptical annulus with center at R.A. = $12^h18^m57^s.505$, decl. = $+47°18'4''.3$, position angle PA = 150°, axis ratio b/a = 0.389 (i.e., $\cos 67°.1$),[18] and inner and outer semimajor axes, respectively, of 6' and 12' (13.3 and 26.5 kpc at the distance of NGC 4258). The projection parameters of the galaxy have been taken from de Vaucouleurs et al. (1991). The HALOGAS moment-1 pixels are 4'' on a side, but the actual resolution is 30''. Given the data quality and depth, the map is reliable to a column density level of $N_{\rm H\,I} = 2 \times 10^{19}$ atom cm^{-2}, at which it has been clipped. Sinusoidal unweighted fits to the projected GC and H I

velocities are shown with, respectively, solid green and dashed black lines.

Table 4 lists the amplitude, phase, and systemic velocity of the fits. While the amplitude is slightly smaller for the GCs,[19] the phases and systemic velocities are virtually identical for the two systems. Moreover, the uncertainty-corrected velocity dispersion of the GC system, $\sigma_{\rm GC}$, goes down from 162.1 to 119.8 km s^{-1} when the H I velocity at its projected position is subtracted from each one of the clusters, and to 99.5 km s^{-1} when the value of the fit to the GC projected velocities is used instead.[20]
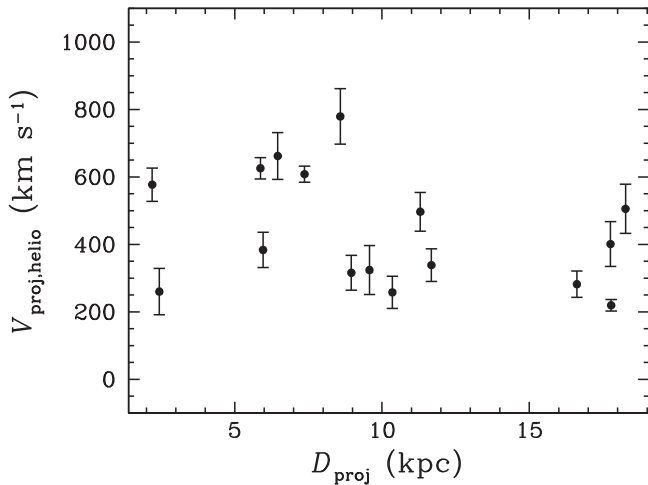
In order to estimate the probability of detecting actual rotation from a sample as small as 16 objects, we simulated various cluster systems with different structure and kinematics, and we examined which one better matched the observations. The radial distribution of the clusters was chosen to reproduce that of the Milky Way GC system. Specifically, we used the Galactocentric radii in Harris (1996) and fitted them with a Lorentzian profile.[21] This function provides a very good fit to the data, far superior to a Gaussian or a power-law distribution.

---

[18] The inclination i is, actually, 68°.3, from $\cos^2 i = [(b/a)^2 - q_0^2]/[1 - q_0^2]$, with $q_0 = 0.13$ (Giovanelli et al. 1994).

[19] We note that the sinusoidal fit to the H I data does not reach the maximum projected velocity of $\sim$203 km s^{-1}.

[20] The average uncertainty of the fit, 88.5 km s^{-1}, was estimated by means of a Monte Carlo simulation, in which we performed 50,000 realizations of the fit around the values of the amplitude, phase, and systemic velocity in Table 4, to probe their Gaussian uncertainties.

[21] $\mathcal{L}(r) = h/\pi[1 + (r/\gamma)^2]$, where $\gamma = 5.72$ kpc, and h is a normalization factor that depends on the number of clusters.
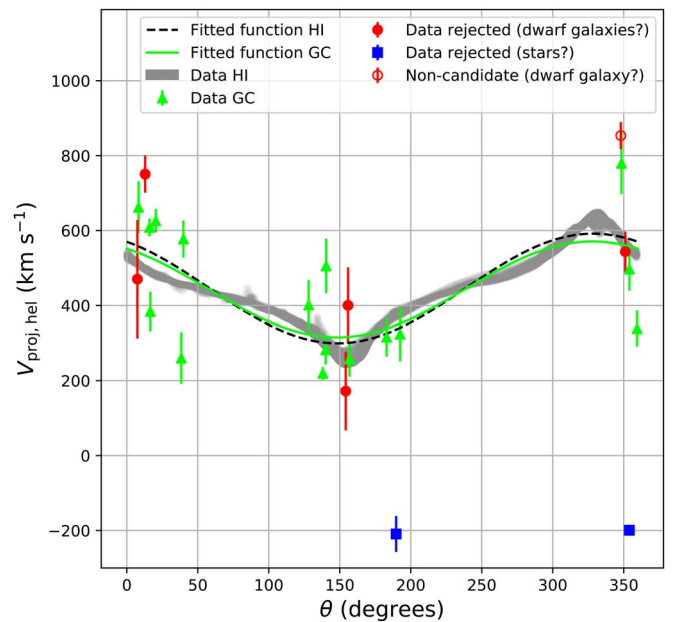
Figure 7. Projected LOS heliocentric velocities of confirmed GCCs vs. projected galactocentric distance.
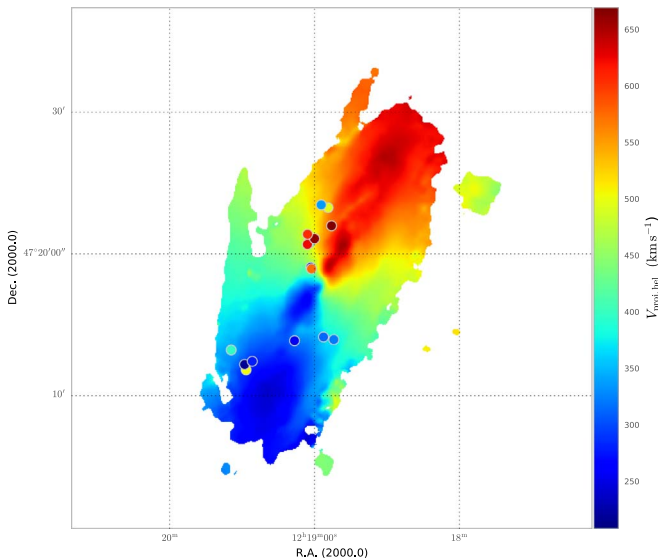
Figure 8. Projected LOS heliocentric velocities of confirmed GCCs (solid circles) and NGC 4258 H I disk. The velocity scale is indicated in the sidebar. This figure was made with the Kapteyn software package.

For the angular distribution, we considered first a system with spherical symmetry, mimicking a spherical halo, and, as a second possibility, a thin disk. Finally, for the kinematics, we worked with two options. First, we used a rotating system with a flat rotation curve with $V_{max} = 220 \, \mathrm{km \, s^{-1}}$ beyond a radius of 1.5 kpc, and a solid body rotation within that radius; superposed on this organized rotation, we added a random component with a dispersion of $10 \, \mathrm{km \, s^{-1}}$ in each of the three directions. The second velocity choice was a random distribution, also with $V_{max} = 220 \, \mathrm{km \, s^{-1}}$. In all cases, we included errors on the simulated radial velocities of 20–$80 \, \mathrm{km \, s^{-1}}$, consistent with the observational errors of the actual data. Summarizing, then, we had three different types of simulations: a random halo, a rotating halo, and a rotating disk.

We ran each kind of simulation 200 times. For every run, we extracted positions on the plane of the sky and radial velocities (i.e., projected along the line of sight) and selected the same number of clusters as in the observations (16), restricted to the two areas where the actual spectroscopic data were obtained

Figure 9. Projected LOS heliocentric velocities vs. azimuthal angle. Green triangles: confirmed GCCs; red circles: rejected candidates (solid) and noncandidates (open), possibly dwarf satellite galaxies of NGC 4258; blue squares: rejected candidates, likely MW foreground stars; thick gray line: H I; solid green line: sinusoidal fit to GCCs; dashed black line: sinusoidal fit to H I.

Table 4
Fits to GC and H I Projected Velocities

System	Amplitude (km s^{-1})	Phase (deg)	Systemic Velocity (km s^{-1})
H I	146.1 ± 0.2	121.6 ± 0.1	445.6 ± 0.2
GCs	127.9 ± 60.9	122.1 ± 45.9	443.1 ± 50.9
GCs+dwarfs	168.1 ± 66.0	132.3 ± 31.2	467.7 ± 44.5

(see right panel of Figure 3). We then fitted the simulated velocities as a function of position angle with a sinusoid, as we did with the real observations. The fits to the observed H I and GC data presented in Figure 9 agree with each other to about an rms of $13 \, \mathrm{km \, s^{-1}}$.[22] We consider that a fit to one realization of the simulations is consistent with the data if it agrees to better than 3σ (defined in the same way as the quoted rms) with the H I fit. We find that this occurs for 51% of the simulations of a rotating disk, for 24% of the realizations for a rotating halo, and only 1% of the time for a halo with randomly distributed velocities (see Figure 10). This exercise indicates that the measured velocities are incompatible with a nonrotating system and are significantly more compatible with a rotating disk than with a rotating spherical system.

Hence, we conclude that there is strong evidence of rotation among the confirmed GC candidates of NGC 4258, and we adopt a value of $\sigma_{GC} = 110 \pm 10 \, \mathrm{km \, s^{-1}}$ (average of the two previous estimates) for the galaxy. We also observe that probable satellite galaxies seem to share the rotation of the GC system. If we include them in the fit to the projected GC velocities, the amplitude actually *increases*, while remaining consistent with the measurement for GCs only, as shown in Table 4. Finally, if these objects are included in the calculation

---

[22] This is the rms of the difference between the two fits, calculated in 1° bins.
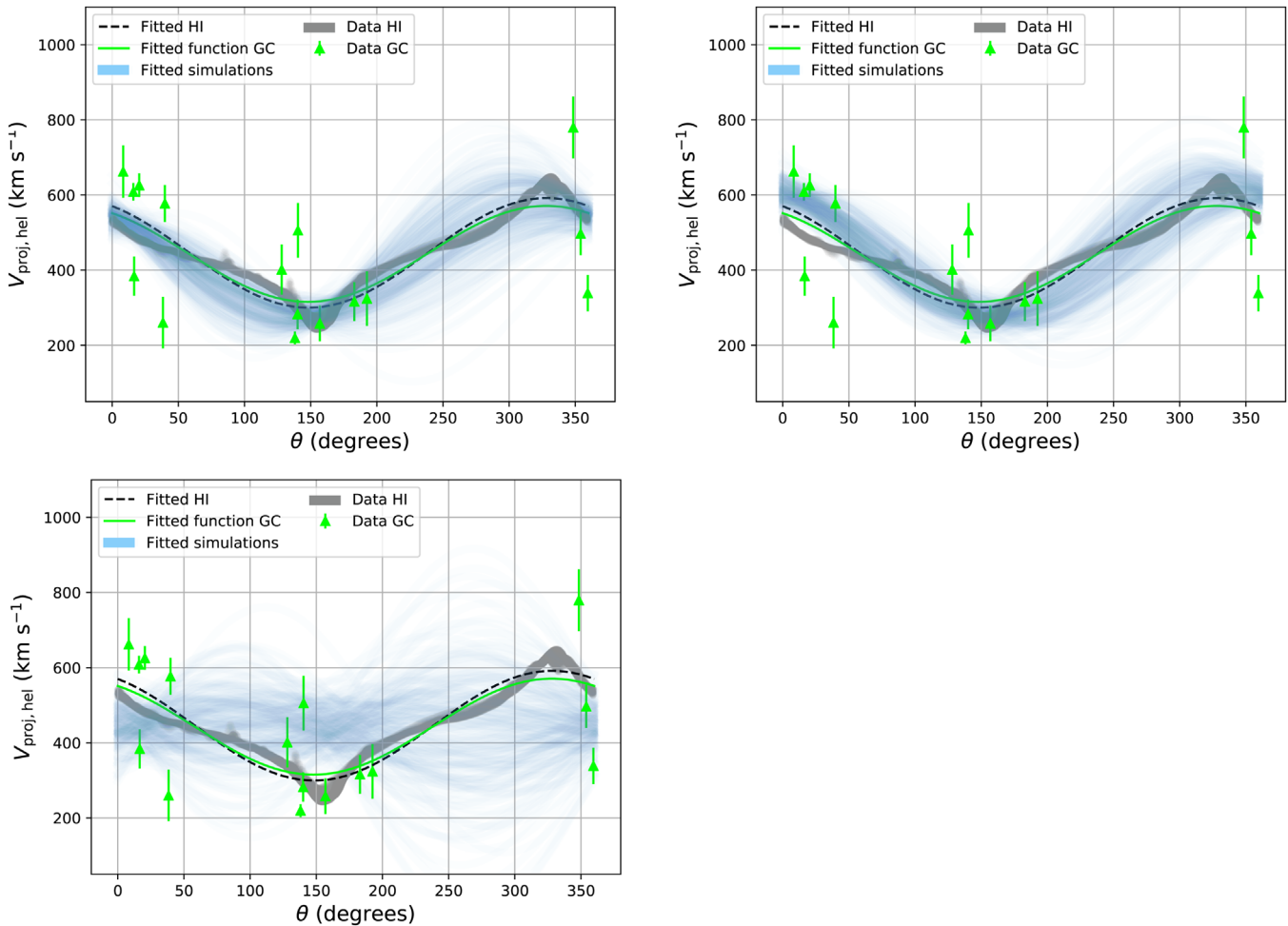
Figure 10. Simulations: projected LOS velocities vs. azimuthal angle for a rotating disk (top left), a rotating halo (top right), and a random halo (bottom left). Thick light-blue lines: sinusoidal fits to 16 "clusters" drawn from the same areas as the spectroscopic data (see the text). Other symbols and lines are as in Figure 9.

of the velocity dispersion, we get $\sigma = 120 \pm 9 \, \mathrm{km \, s^{-1}}$, consistent with the measurement without them.

We can now compare the measured rotation-corrected velocity dispersion of the GC system to the expected σ_{GC} from the correlation with the central supermassive black hole mass ($M_\bullet$) derived by Sadoun & Colin (2012). These authors find $\log \, (M_\bullet) = \alpha + \beta \log \, (\sigma_{GC}/200 \, \mathrm{km \, s^{-1}})$, with $\alpha = 8.63 \pm 0.09$ and $\beta = 3.76 \pm 0.52$. Taking $M_\bullet = (4.00 \pm 0.09) \times 10^7 \, M_\odot$ (Humphreys et al. 2013) and propagating the errors in both the correlation coefficients and the $M_\bullet$ measurement, we find the expected velocity dispersion is $\sigma_{GC} = 107 \pm 13 \, \mathrm{km \, s^{-1}}$, which is in excellent agreement with the value of $110 \pm 10 \, \mathrm{km \, s^{-1}}$ we derived.

5. Metallicity

As a result of the generally low S/N, we did not attempt to estimate the ages and metallicities of the GC candidates from their individual spectra. Instead, we stacked the spectra of all of the confirmed GC candidates into a single spectrum, and hence derived a mean age and metallicity for the GC population. To this end, we used the penalized pixel-fitting algorithm (pPXF; Cappellari & Emsellem 2004), which extracts stellar population properties by fitting a linear combination of different templates to an observed spectrum in pixel space. The available templates are 182 solar-scaled isochrones with a Salpeter initial mass

function (IMF), initial masses from $0.15 \, M_\odot$ to $7 \, M_\odot$, a range of metallicity $-2.3 < [M/H] < 0.2$, a helium fraction of $Y = 0.23 + 2.25Z$, and ages between 1 and 17 Gyr. The isochrones also incorporate the thermally pulsing asymptotic giant branch (AGB) regime to the point of complete envelope ejection (Girardi et al. 2000).

Before stacking, each individual GCC spectrum was multiplied by a mask with a value of zero in noisy regions and one otherwise;[23] the coadded spectrum was divided by the sum of the masks, then normalized to a maximum value of 1. The resulting spectrum, in rest wavelength, is shown in Figure 11; in view of the improved S/N (~80) with respect to the individual GCC spectra, we did not apply additional smoothing.

Given the lack of a perfect flux calibration along the full spectral range, we carried out separate fits in windows 200 Å wide around the Mg b triplet and Hα, respectively, a metallicity-sensitive indicator and a widely used age-sensitive feature. For each region, a first pPXF fit was performed in order to estimate the noise factor, such that multiplied by the noise one would obtain a reduced χ^2 (χ^2 per degree of freedom) = 1. No polynomial (neither multiplicative nor additive) was included in the fit, because the continuum shape contains

---

[23] Noisy regions are those also excluded from the Fourier cross-correlation for the radial velocity estimate.
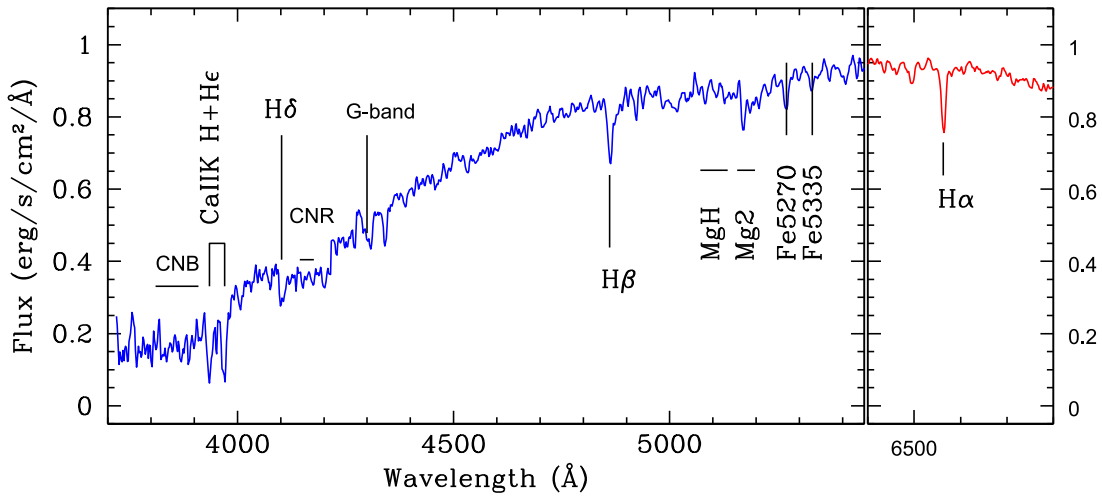
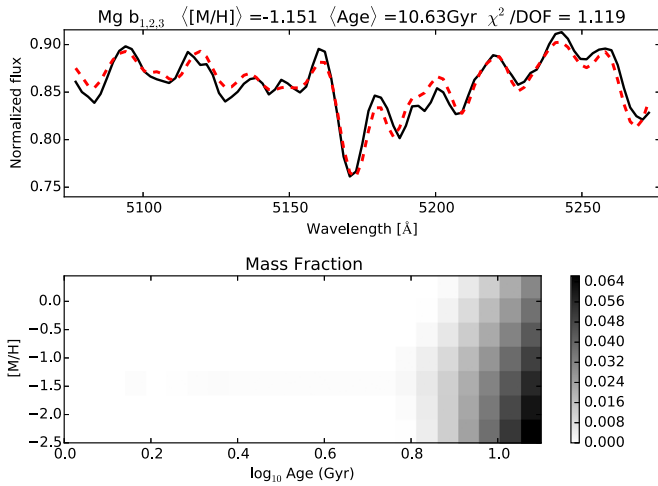**Figure 11.** Stacked, normalized spectrum of confirmed GC candidates.

Figure 12. Mass-weighted metallicity and age of the GC system from the fit to the Mg b triplet spectral window. Top: observed (black solid line) and model (red dashed line) spectra; bottom: mass fraction distribution as a function of age and metallicity (grayscale). The derived [M/H] and age, as well as the reduced χ^2, are written above the top panel.

important information about the population (Cappellari & Emsellem 2004; Wolf et al. 2007). Subsequently, a second iteration of the fit was done with the previously obtained noise factor and with linear regularization (smoothing) of the weights in the age and metallicity axes; both the continuum and the absorption features were fit, assuming constant noise per pixel. Milky Way foreground extinction was not considered, given its very low value of $A_V = 0.04$ (Schlafly & Finkbeiner 2011) in the line of sight toward NGC 4258.

In Figures 12 and 13, we show the best fit for the two spectral regions and their corresponding mass fraction distributions as a function of age and metallicity. The values above the top panels are mass-weighted metallicity [M/H] and age. We note that the mass fraction distribution with metallicity is quite different for the two spectral windows. In the case of the Mgb index, it is very extended and goes from 1/20 solar to supersolar; almost half (44%) of the mass has [M/H] > -1.2. For Hα, the mass distribution is significantly narrower in [M/H]. However, the mass-weighted mean metallicities are very similar for both ranges. While there are limitations of the
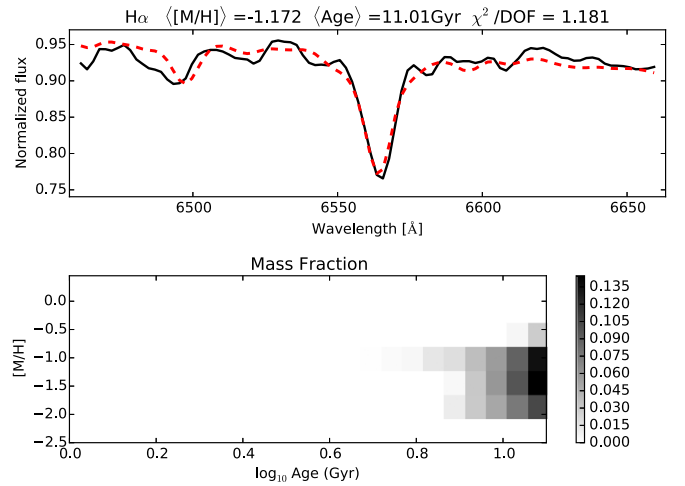

Figure 13. Mass-weighted metallicity and age of the GC system from the fit to the Hα spectral window. Panels as in Figure 12.

data and the models (the resolution can modify absortion features, calibration of wavelength and continuum, fraction of blue stragglers, among others) and we cannot set strong constraints on the age or the metallicity, we can certainly conclude that the recovered populations are old ($\sim$11 Gyr) and metal-poor ($\langle$[M/H]$\rangle \sim -1.2$).

6. Photometric Method Validation and the N_{GC} versus $M_\star$ Correlation

Our spectroscopic observations of about half the total sample of NGC 4258 GCCs show 16 confirmed candidates, 10 confirmed noncandidates, and seven rejected candidates, that is, no false negatives and a sample contamination of 30%. The seven contaminants are fully consistent with the results of Powalka et al. (2016), who found, with the $u^*i'K_s$ technique, between 50 and 100 contaminants among the GCCs of M87, in a FOV nine times larger. Both M87 and NGC 4258 lie at high Galactic latitudes (respectively, $b = 74\overset{\circ}{.}5$ and $b = 68\overset{\circ}{.}8$), and indeed the Besançon model of Galactic structure (Robin & Creze 1986) predicts an almost equal number of foreground stars in their lines of sight (355 versus 329 brighter than apparent $u = 20$ mag within one square degree). The number of background galaxies, on the other
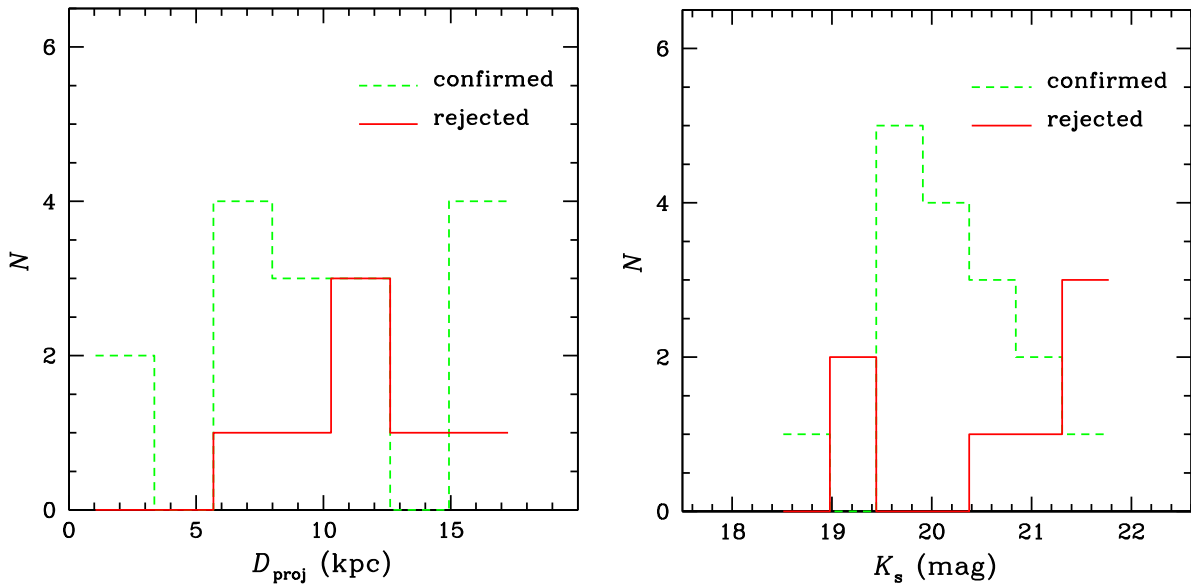
Figure 14. Distributions of confirmed (green dashed lines) and rejected (red solid lines) candidates. Left: galactocentric projected distances; right: K_s-band magnitudes.

hand, should be about the same, within a few times the Poisson error (e.g., Ellis & Bland-Hawthorn 2007).

The left panel in Figure 14 displays the distributions of galactocentric projected distances of both confirmed (dashed green line) and rejected (solid red line) candidates; the latter lie on average slightly farther away than most confirmed GCCs, so crowding and background light should not be important contributing factors to contamination. Figure 15 shows the FWHM (top left), SPREAD_MODEL ($\times 100$; top right), axis ratios (middle left), K_s magnitude values (middle right), ($u^* - i'$) (bottom left), and ($i' - K_s$) (bottom right) colors of the confirmed (green bars) and rejected (red bars) candidates. GLL J121905+472422 has both the largest FWHM and SPREAD_MODEL and the bluest ($u^* - i'$) and ($i' - K_s$) colors; together with GLL J121854+472245, it is also among the three brightest objects in the K_s band. GLL J121910+471343 has the second largest SPREAD_MODEL value, whereas GLL J121903+472613 holds the second bluest ($u^* - i'$) and ($i' - K_s$) colors. GLL J121854+472144 has an axis ratio of 0.63, which is clearly smaller than the minimum observed axis ratio of 0.7 for the GCs in both the MW (White & Shawl 1987) and M31 (Lupton 1989). The inclusion of GLL J121854 +472144 in our sample was definitely an oversight, because we had actually measured the axis ratios of our candidates with GALFIT (Peng et al. 2010). Given the shallowness of our near-infrared data of NGC 4258, we hesitate at this point to propose moving the faint cut in K_s to a brighter limit. However, a histogram of the K_s magnitudes of the confirmed and rejected candidates (Figure 14, right panel) indicates they do have different distributions, and the middle right panel of Figure 15 shows that three rejected candidates cluster around $K_s = 21.4$; only one confirmed GCC is fainter. Of the three very faint rejected candidates, GLL J121909+471335 alone does not stand out as a near-outlier in any other gauge (GLL J121903 +472613 is quite blue and GLL J121854+472144 has a small axis ratio). Finally, GLL J121852+471313 is the singular unremarkable source in every one of the inspected parameters.

We could easily depurate the sample of five (out of seven) spurious candidates, while losing only one confirmed GC, by

slightly changing the limits of our selection parameters in future works. As indicated by the dashed lines, we would suggest using SPREAD_MODEL $\leqslant 0.015$, axis ratio $\geqslant 0.7$, LFTO—2 (or LFTO—1.7 σ_{LFTO}) $\leqslant$ MAG_AUTO[24] $\leqslant$ LFTO + 3 σ_{LFTO}, FWHM $\leqslant$ 29 pc, ($u^* - i'$) $\lesssim 1.54$, and ($i' - K_s$) $\lesssim -0.11$.

From their final sample of 39 GC candidates, and considering two (5%) contaminants, González-Lópezlira et al. (2017) extrapolated to a total of $N_{\text{GC}} = 144 \pm 31^{+38}_{-36}$ for NGC 4258, with the first error statistical and the second systematic. These numbers were obtained following the procedure introduced by Kissler-Patig et al. (1999). The method, based on a comparison with the GC system of the MW, simultaneously accounts for photometric incompleteness, extrapolation over the luminosity function, and incomplete spatial coverage. The total number of clusters in a galaxy, N_{GC}, is equal to the number of MW clusters, multiplied by the ratio of the observed GCCs to the numbers that would have been detected in the MW if our Galaxy were observed at the distance and with the orientation of the galaxy of interest, with the same instrument and to the same depth.

Here, applying the 30% contamination correction to the total number, total mass, and specific frequency derived by González-Lópezlira et al. (2017) for the GC system of NGC 4258, we arrive at $N_{\text{GC}} = 105 \pm 26 \pm 31$, log $M_{\text{GC}} = 7.5 \pm 0.1 \pm 0.1$, and $S_N = 0.3 \pm 0.1$ (random uncertainty only). After the contamination correction, NGC 4258 is in even closer agreement than estimated by González-Lópezlira et al. (2017) with the scaling relations between GC system parameters and $M_\bullet$ derived for elliptical galaxies.[25]

7. Discussion and Conclusions

Using MOS, we have investigated both the validity of the $u^* i' K_s$ method and light-concentration parameters to select

---

[24] Kron-like (Kron 1980) elliptical aperture magnitude measured by SExtractor.
[25] The relations can be written as log $N_{\text{GC}} = (-5.78 \pm 0.85) + (1.02 \pm 0.10)$ log $M_\bullet/M_\odot$ and log $M_{\text{GC}} = (-1.40 \pm 0.79) + (1.15 \pm 0.09)$ log $M_\bullet/M_\odot$. For the mass of the central black hole of NGC 4258, these correspond to $N_{\text{GC}} = 100$ and log $M_{\text{GC}} = 7.3$.
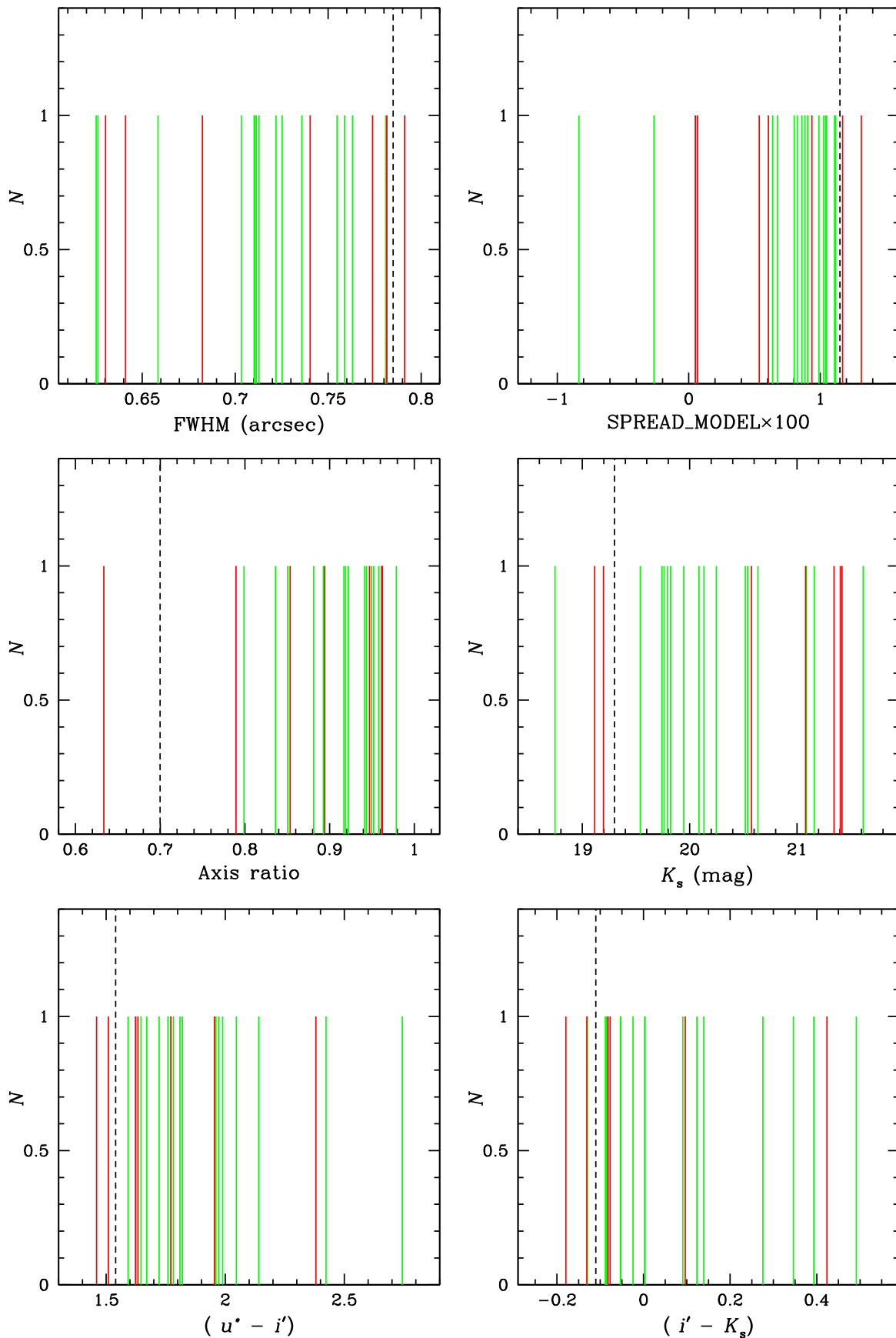
Figure 15. Sample selection parameters. Top left: FWHM; top right: SPREAD_MODEL × 100; middle left: axis ratio; middle right: K_s magnitude; bottom left: $(u^* - i')$; bottom right: $(i' - K_s)$. Green bars: confirmed GCCs; red bars: rejected GCCs. Dashed lines: suggested new value limits for improved selection.

GCC samples in spiral galaxies, and the kinematics of the GC system of the megamaser prototype NGC 4258.

Regarding the $u^*i'K_s$ method, we have confirmed that it works very efficiently for spirals, with the only (expected) limitation that the fractional contamination will be slightly higher than for ellipticals, given the sparser GC systems of disk galaxies. In our working case, there were no false negatives, and the absolute number of contaminants in the sample was consistent with the Galactic latitude of the observed field and the cosmic variance of background galaxies. We suggest here a few distance-independent refinements to the limits on the light-concentration parameters and magnitude values used for the sample selection that should help reduce contamination by 30%–50%.

Once corrected for contamination, NGC 4258 falls right on the N_{GC} and M_{GC} (total mass of the GC system) versus $M_\star$ relations followed by elliptical galaxies, within significantly less than 1σ.

We have also determined that the GC system seems to actually have a disky configuration and to be rotating with a projected maximum velocity of $128\,\mathrm{km\,s^{-1}}$, in phase with the H I disk. This merits further investigation, for example, through a full dynamical modeling. In a few GC systems for which rotation has been measured, it is most common for the metal-rich population (MRP) with small real or projected galactocentric distances. For example, in the MW,[26] the MRP ([Fe/H] = -0.6) within 9 kpc from the Galaxy center has an average rotation velocity $V_{\mathrm{rot,MRP}} = 116 \pm 24\,\mathrm{km\,s^{-1}}$ ($\sim$50% of disk rotation; Reid et al. 2014) and a ratio $V_{\mathrm{rot,MRP}}/\sigma_{\mathrm{LOS,MRP}} = 1.4 \pm 0.3$, where σ_{LOS} is the line-of-sight velocity dispersion. However, the metal-poor population (MPP; [Fe/H] = -1.6) is pressure supported, with an average $V_{\mathrm{rot,MPP}} = 31 \pm 26\,\mathrm{km\,s^{-1}}$ and $V_{\mathrm{rot,MPP}}/\sigma_{\mathrm{LOS,MPP}} = 0.3 \pm 0.3$ between 0 and 12 kpc.

On the other hand, in M81 (Nantais & Huchra 2010), the MRP ([Fe/H] > -1.06) lies mostly within 4 kpc from the center and has $V_{\mathrm{rot,MRP}} = 122 \pm 18\,\mathrm{km\,s^{-1}}$ ($\sim$60% of disk rotation; Faber & Gallagher 1979) and $V_{\mathrm{rot,MRP}}/\sigma_{\mathrm{LOS,MRP}} = 1$, whereas the MPP ([Fe/H] < -1.06) reaches beyond 8 kpc and is, once again, pressure supported, with $V_{\mathrm{rot,MPP}} = 67 \pm 38\,\mathrm{km\,s^{-1}}$ and $V_{\mathrm{rot,MPP}}/\sigma_{\mathrm{LOS,MPP}} = 0.5$. In M31, Lee et al. (2008) find that the MRP ([Fe/H] = -0.6) rotates within 3 kpc with an average $V_{\mathrm{rot,MRP}} = 221 \pm 35\,\mathrm{km\,s^{-1}}$ ($\sim$95% of disk rotation; Faber & Gallagher 1979) and $V_{\mathrm{rot,MRP}}/\sigma_{\mathrm{LOS,MRP}} = 1.9 \pm 0.3$. In addition, Perrett et al. (2002) noticed that the MRP of M31 is not flattened and hence is bulge-like, that its rotation axis is tilted $5°$–$10°$ with respect to the minor axis of M31, and that its velocity dispersion is quite similar to the bulge's. Beyond 3 kpc, there is no evidence of rotation for the metal-rich clusters. The MPP in M31 rotates with basically the same speed as the MRP, $V_{\mathrm{rot,MPP}} = 217 \pm 33\,\mathrm{km\,s^{-1}}$, to a projected distance of 5 kpc, albeit with a slightly larger velocity dispersion, that is, $V_{\mathrm{rot,MPP}}/\sigma_{\mathrm{LOS,MPP}} = 1.6 \pm 0.5$. Farther away than 5 kpc, the MPP in M31 is pressure supported, with $V_{\mathrm{rot,MPP}}/\sigma_{\mathrm{LOS,MPP}} = 0.7 \pm 0.7$.

The GC system of NGC 4258 is different. It does not have strong signs of bimodality (González-Lópezlira et al. 2017); its members seem to have low metallicity, around $Z = 0.001$ ([Fe/H] ~ -1.2); its spatial distribution seems flattened; and its projected rotation velocity of $128\,\mathrm{km\,s^{-1}}$ is $\sim$65% of the projected H I disk rotation velocity, up to a projected distance of more than 17 kpc. Assuming that the GC system has an intrinsic anisotropy similar to the H I disk and that the viewing angle is the same, the deprojected velocity would be $V_{\mathrm{rot}} \sim 140\,\mathrm{km\,s^{-1}}$ and $V_{\mathrm{rot}}/\sigma_{GC} = 1.3$; without deprojection, $V/\sigma = 1.2$.

These characteristics evoke the clumpy, gaseous, high-pressure disks at $z \geqslant 2$ that constitute nowadays the more favored environment for GC formation (e.g., Agertz et al. 2009; Kruijssen 2015). These disks rotate but are highly turbulent, with $V/\sigma \sim 1$, and their existence is supported by strong observational evidence (e.g., Förster Schreiber et al. 2009; Wisnioski et al. 2015; Harrison et al. 2017; Turner et al. 2017; Dessauges-Zavadsky & Adamo 2018).

Beyond validating the $u^*i'K_s$ plus light-concentration parameter method for the identification of GCCs in spirals, the present work highlights the importance of studying GC systems and scaling relations in spirals. While these relations in ellipticals seem to be showing the end result of star formation and galaxy assembly, in lower mass galaxies we may be witnessing the fingerprints of the individual steps of the process, and hence fundamental clues to the understanding of galaxy formation.

Appendix

OSIRIS spectra and *HST* grayscales of most observed sources have been placed in this appendix for a better flow of the main text (Figures 16–18).

---

[26] https://ned.ipac.caltech.edu/level5/Harris2/Harris1.html
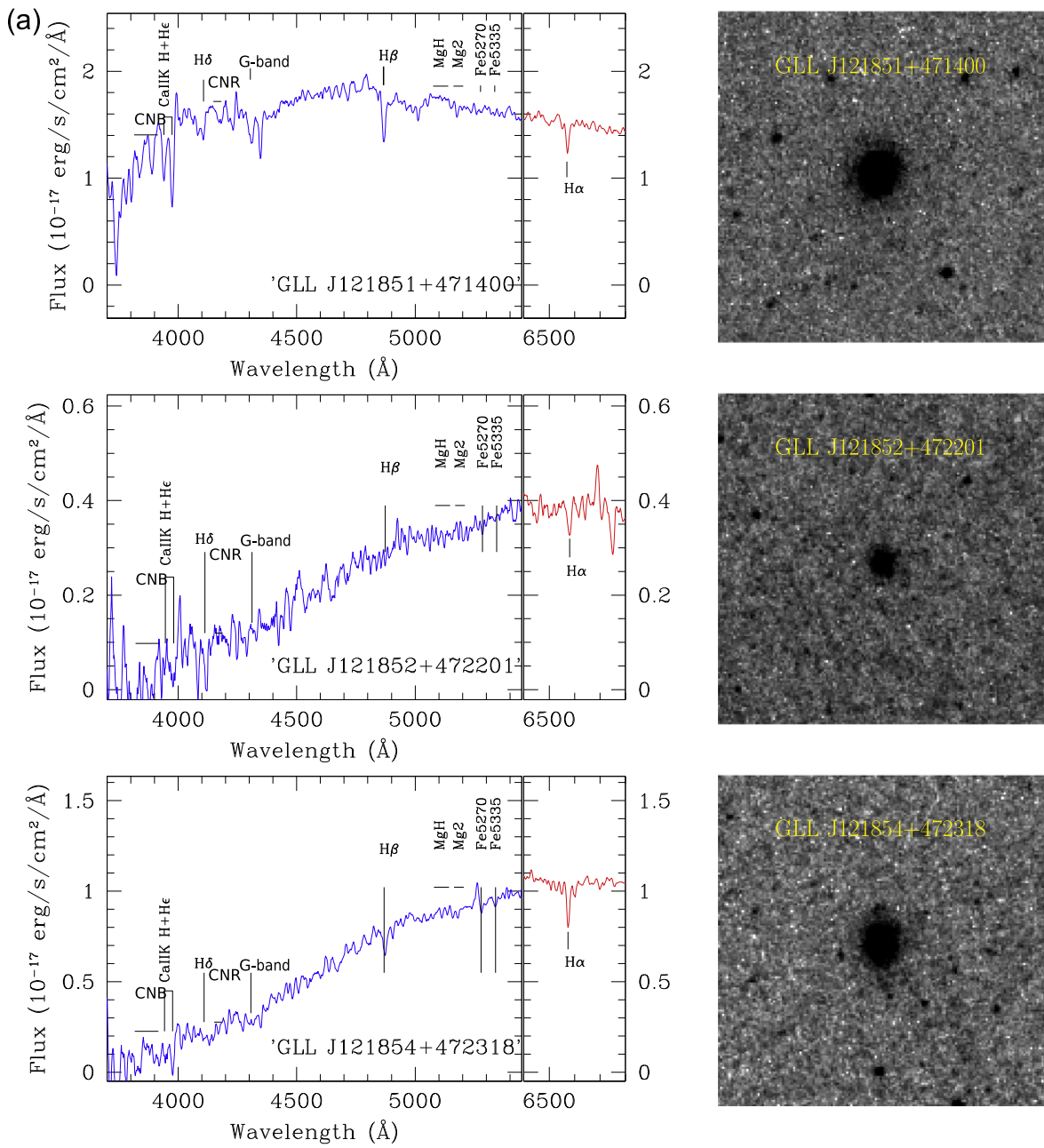
Figure 16. OSIRIS spectra (left) and *HST* grayscales (right) of confirmed GC candidates.
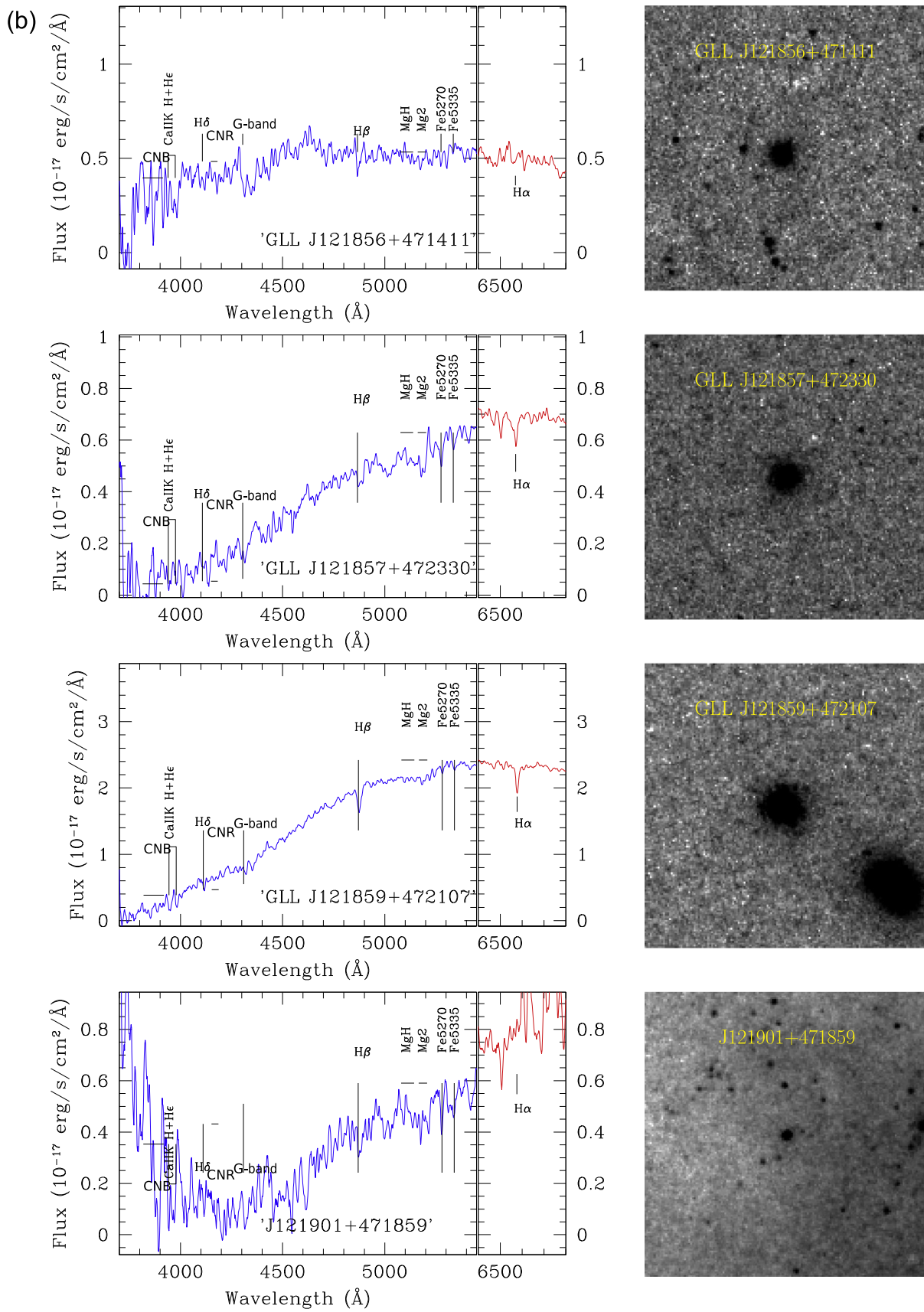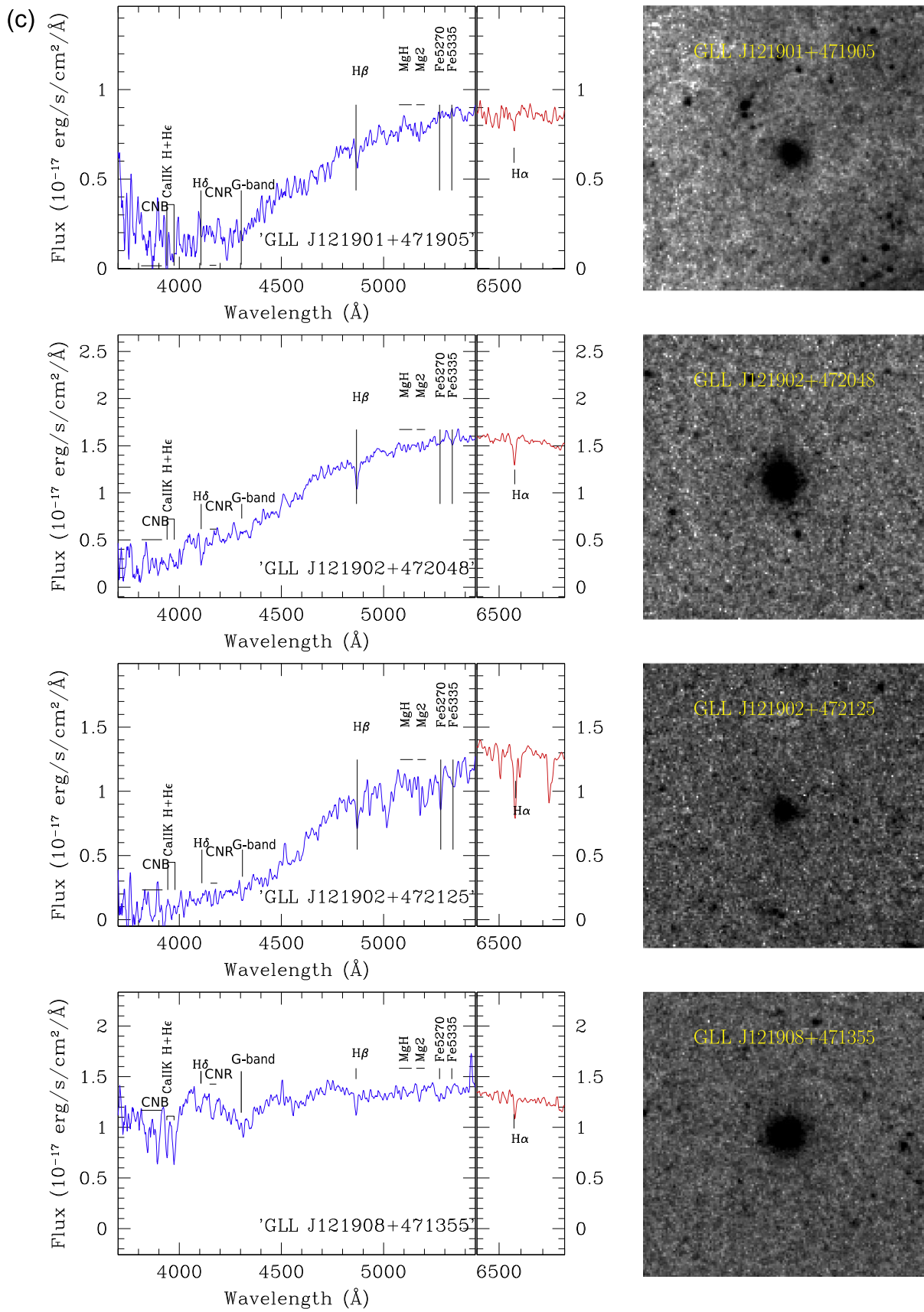
Figure 16. (Continued.)
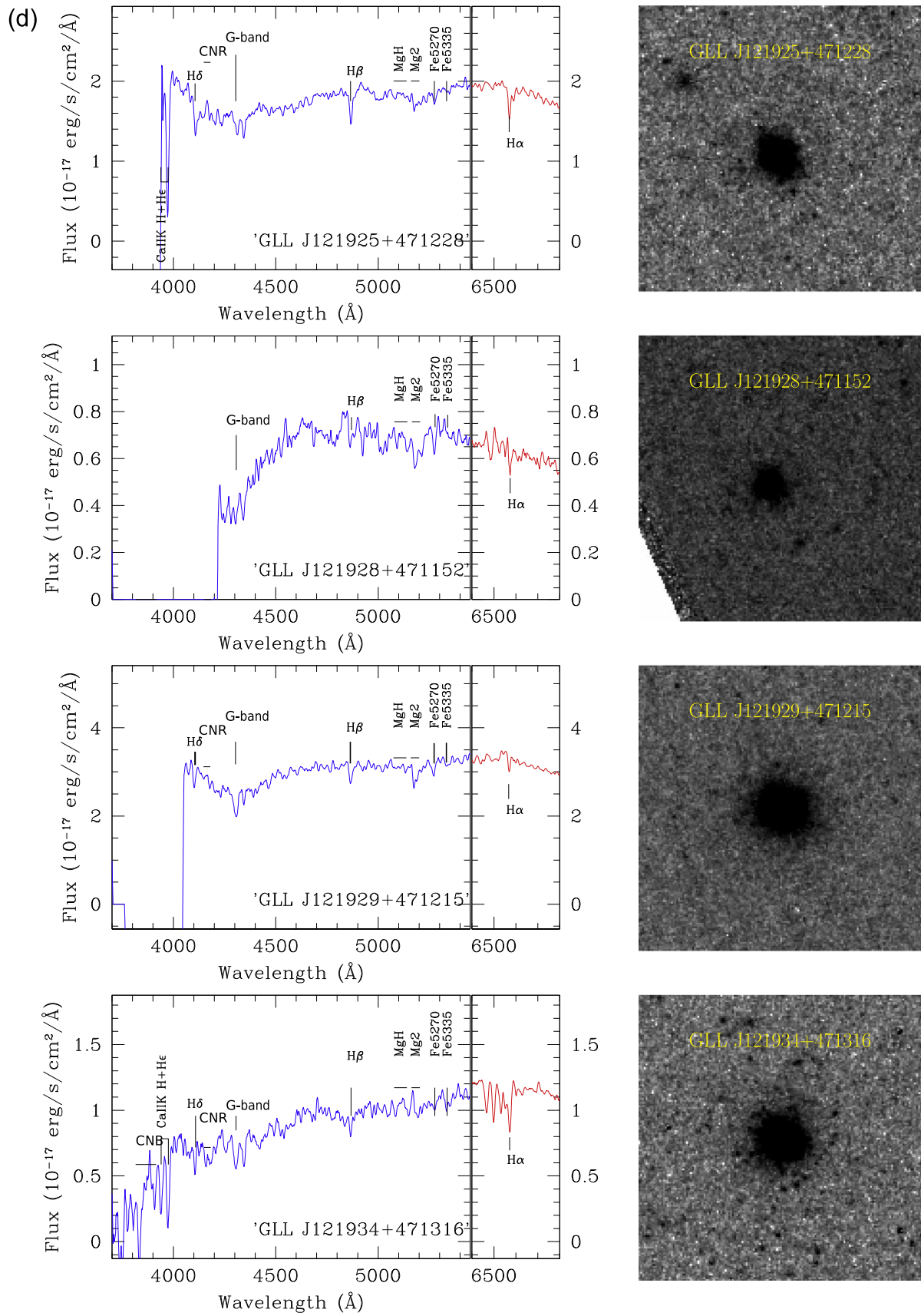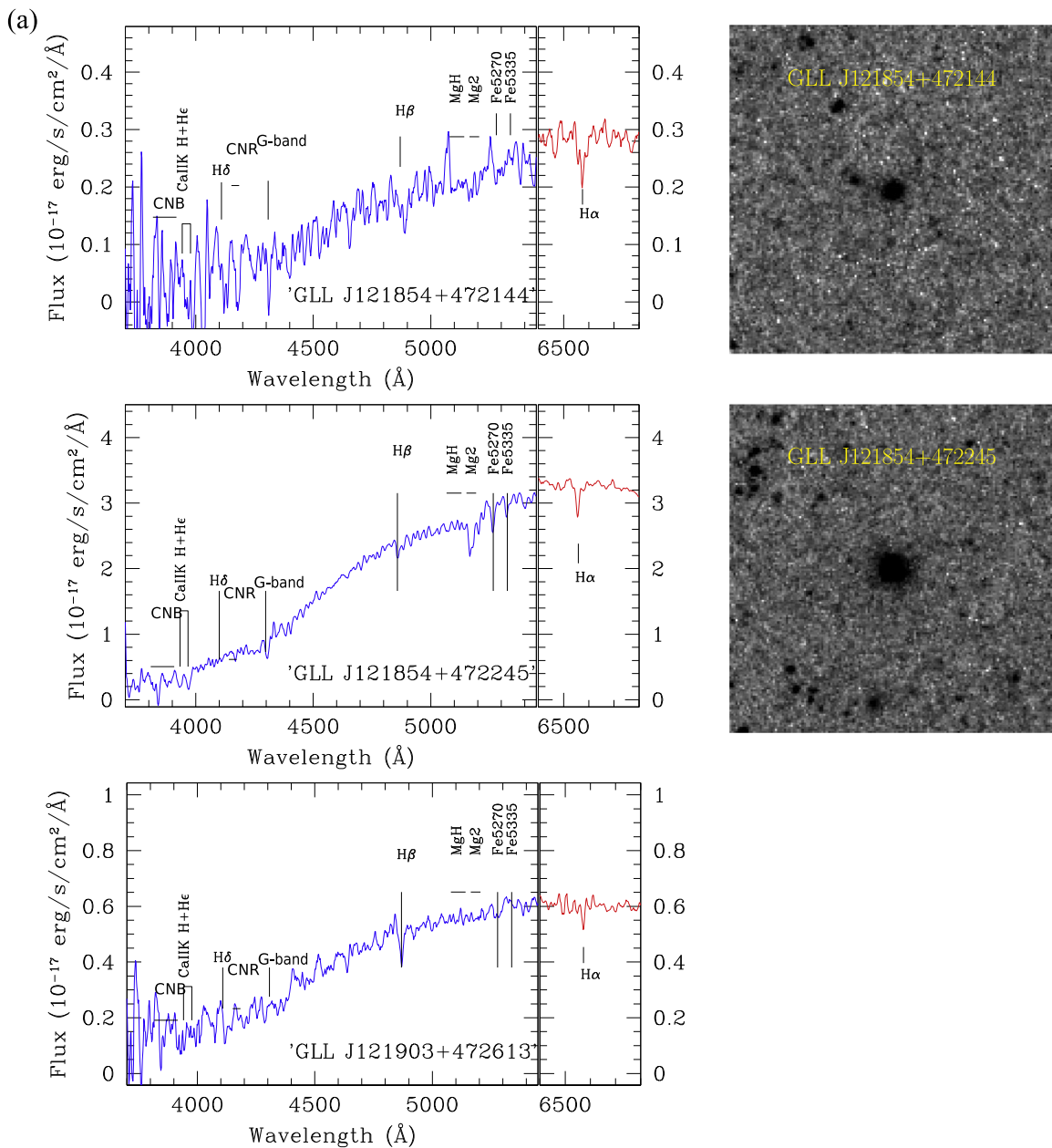
(c)

Figure 16. (Continued.)

Figure 16. (Continued.)

Figure 17. OSIRIS spectra (left) and *HST* grayscales (right) of rejected GC candidates. The spectrum of GLL J121854+472144 (a, top) correlates best with *fm32temp*, a non-GC template. The spectrum of GLL J121854+472245 (a, middle) correlates best with *fm32temp*, a non-GC template, and displays a negative radial velocity; the source is not resolved in the ACS images. The spectrum of GLL J121903+472613 (a, bottom) does correlate with *fglotemp*, a GC template, but only if restricted to wavelengths bluer than 5500 Å; there is no *HST* image of the source. The spectrum of GLL J121905+472422 (b, top) correlates best with *fm32temp*, a non-GC template. The spectrum of GLL J121909+471335 (b, middle) correlates best with *eltemp*, a non-GC template. GLL J121910+471343 (b, bottom) looks quite elongated in *HST* images.
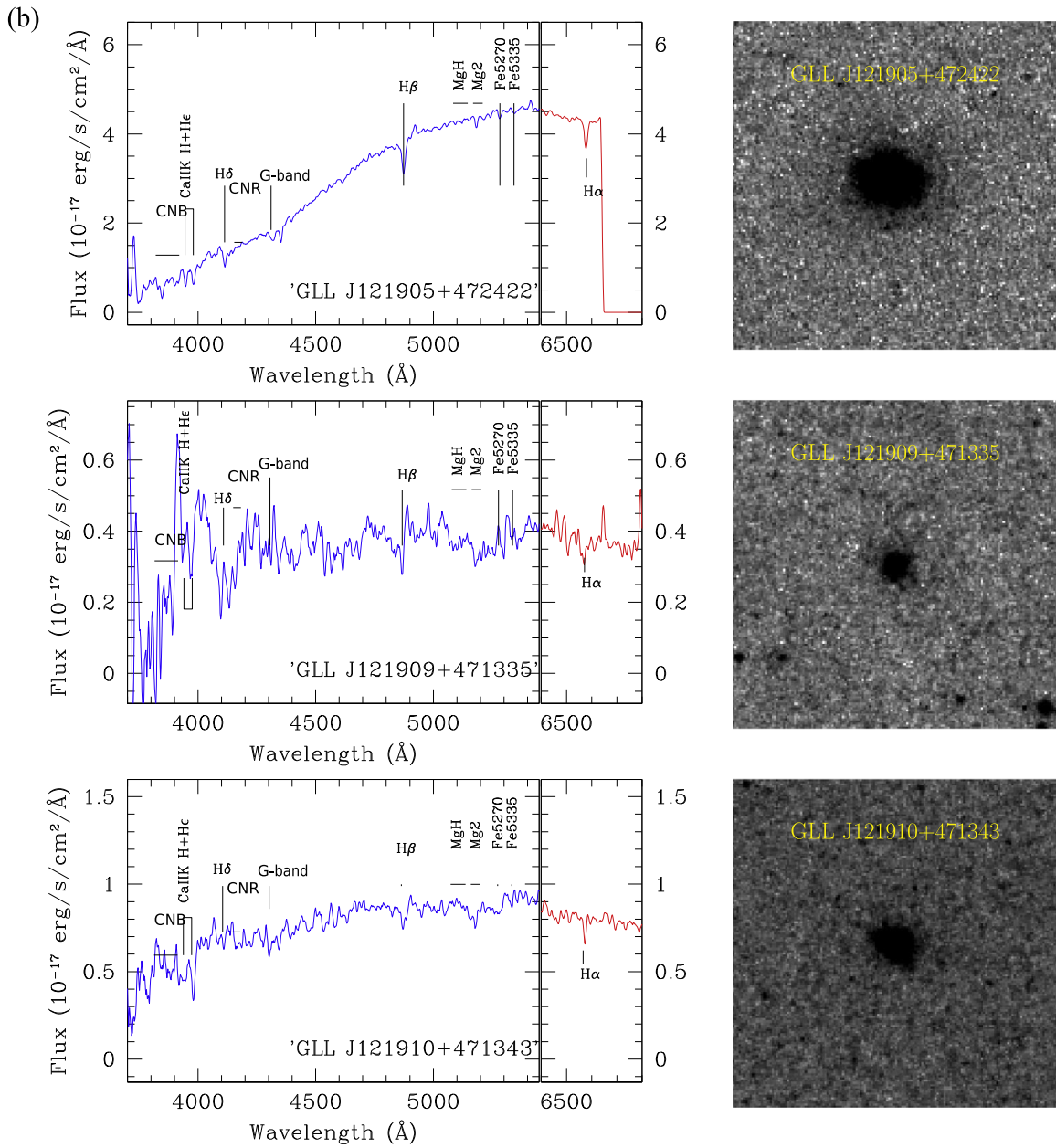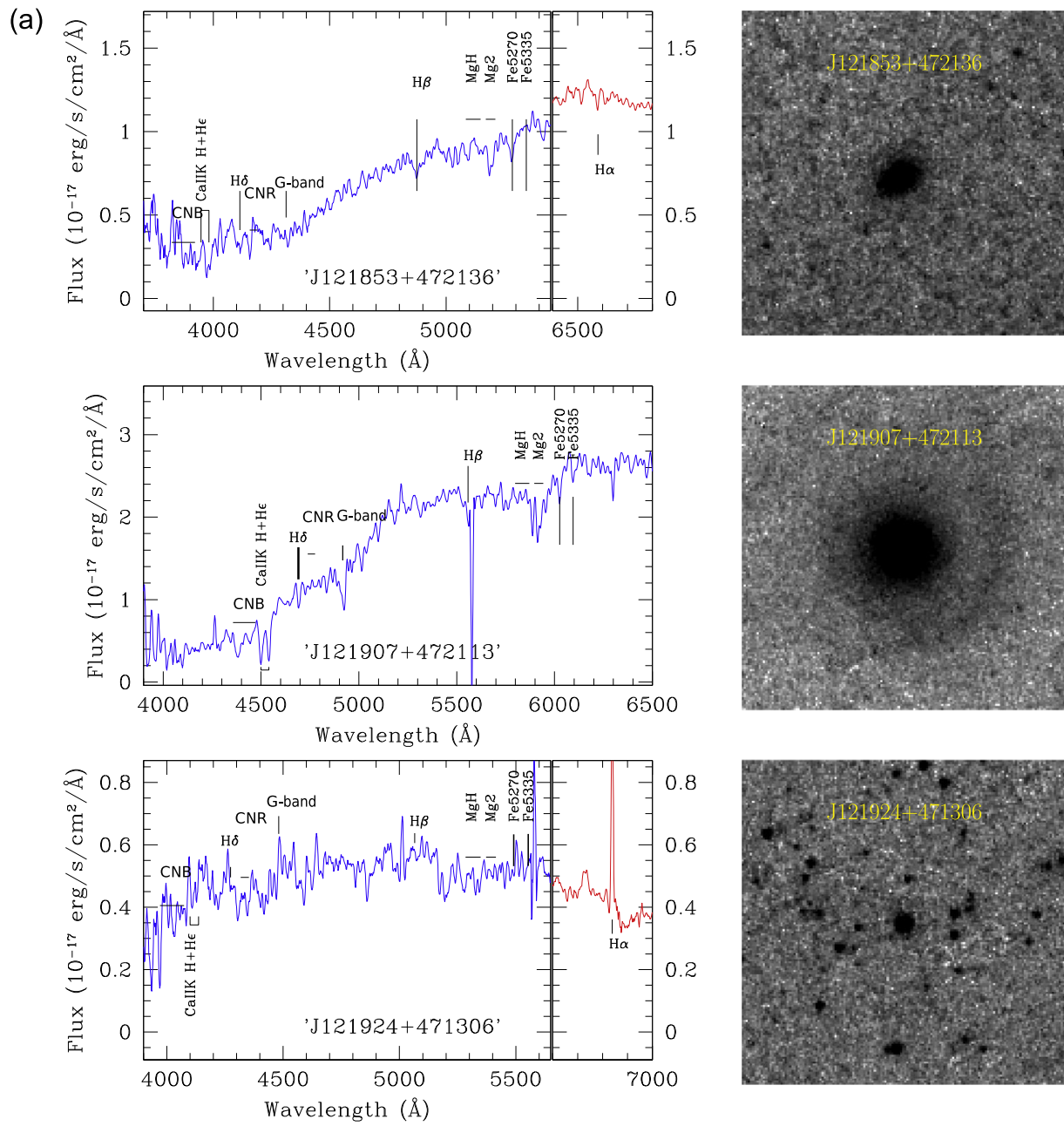
(b)

Figure 17. (Continued.)

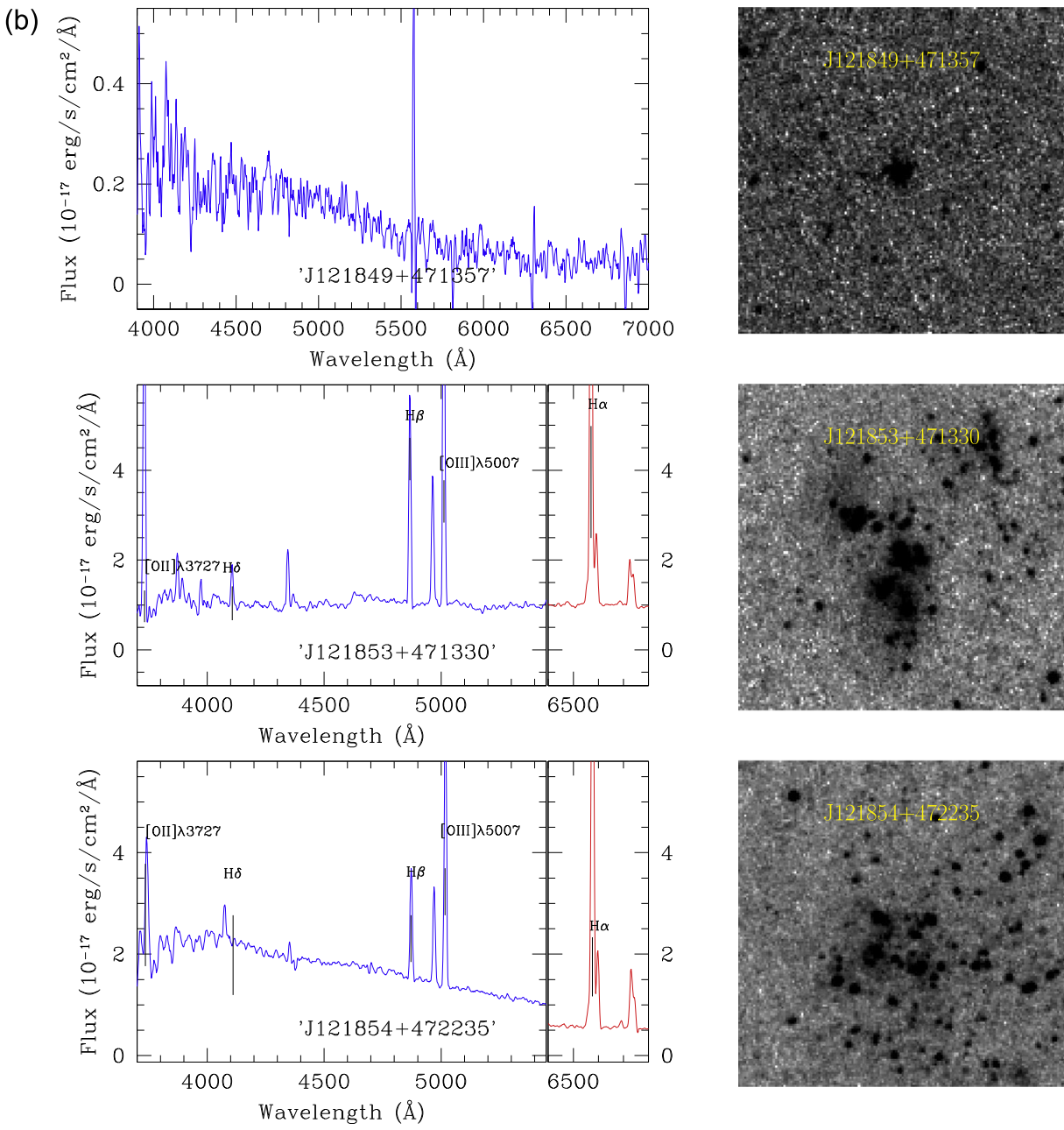**Figure 18.** OSIRIS spectra (left) and *HST* grayscales (right) of noncandidates.
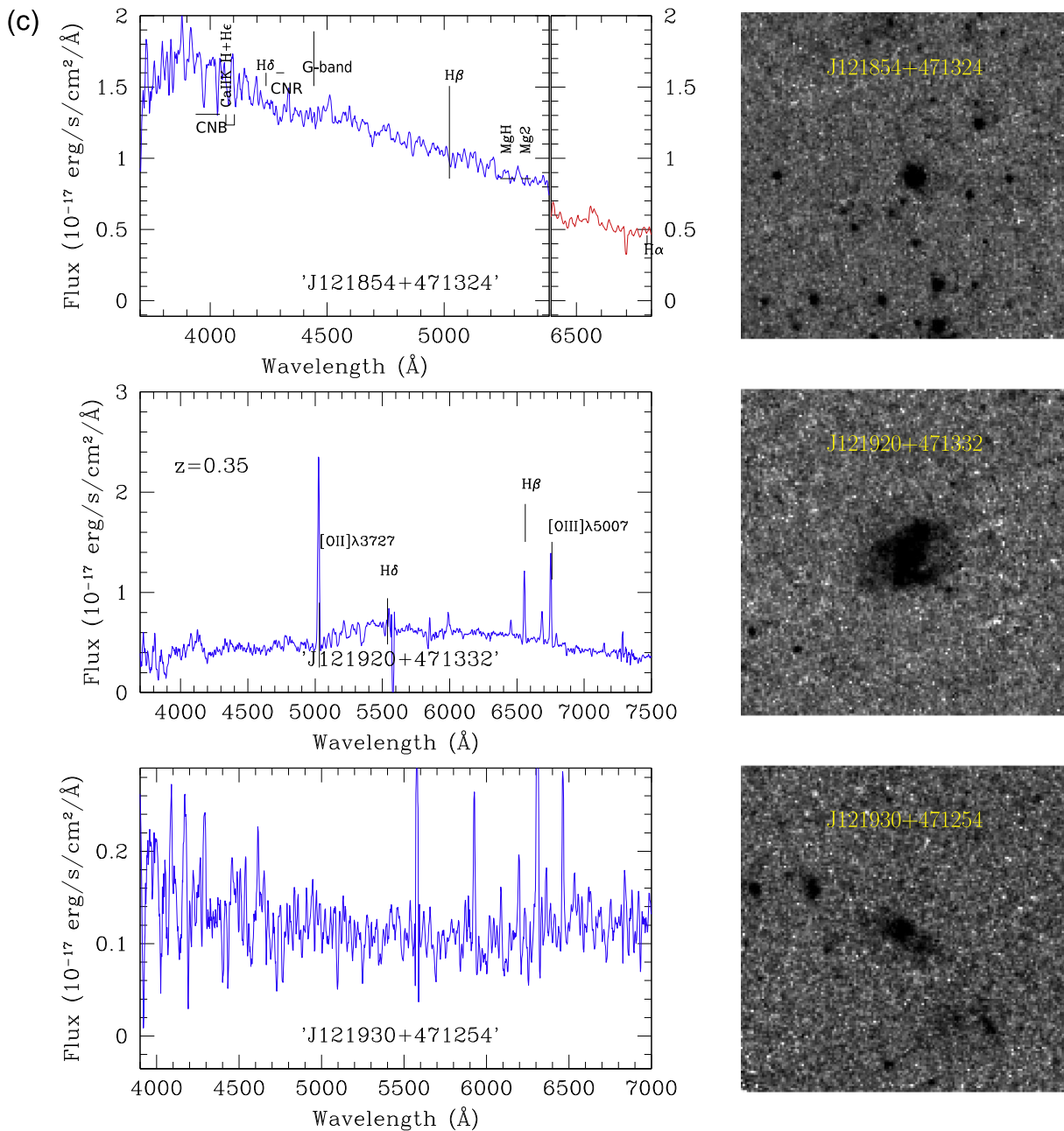
Figure 18. (Continued.)

(c)

Figure 18. (Continued.)

ORCID iDs

Rosa A. González-Lópezlira ⓘ https://orcid.org/0000-0003-1557-4931

Y. D. Mayya ⓘ https://orcid.org/0000-0002-4677-0516

Laurent Loinard ⓘ https://orcid.org/0000-0002-5635-3345

Yasna Órdenes-Briceño ⓘ https://orcid.org/0000-0001-7966-7606

Gustavo Bruzual ⓘ https://orcid.org/0000-0002-6971-5755

Thomas H. Puzia ⓘ https://orcid.org/0000-0003-0350-7061

References

Agertz, O., Teyssier, R., & Moore, B. 2009, MNRAS, 397, L64
Bertin, E., & Arnouts, S. 1996, A&AS, 117, 393
Bruzual, G., & Charlot, S. 2003, MNRAS, 344, 1000
Burkert, A., & Tremaine, S. 2010, ApJ, 720, 516
Cappellari, M., & Emsellem, E. 2004, PASP, 116, 138
Dekel, A., Sari, R., & Ceverino, D. 2009, ApJ, 703, 785
Desai, S., Armstrong, R., Mohr, J. J., et al. 2012, ApJ, 757, 83
Dessauges-Zavadsky, M., & Adamo, A. 2018, MNRAS, 479, L118
Dessauges-Zavadsky, M., Zamojski, M., Schaerer, D., et al. 2015, A&A, 577, A50
de Vaucouleurs, G., de Vaucouleurs, A., Corwin, H. G., Jr., et al. 1991, Third Reference Catalogue of Bright Galaxies, Vol. I, II, and III (New York: Springer)
Ellis, S. C., & Bland-Hawthorn, J. 2007, MNRAS, 377, 815
Faber, S. M., & Gallagher, J. S. 1979, ARA&A, 17, 135
Förster Schreiber, N. M., Genzel, R., Bouché, N., et al. 2009, ApJ, 706, 1364
Georgiev, I. Y., Puzia, T. H., Goudfrooij, P., & Hilker, M. 2010, MNRAS, 406, 1967
Giovanelli, R., Haynes, M. P., Salzer, J. J., et al. 1994, AJ, 107, 2036
Girardi, L., Bressan, A., Bertelli, G., & Chiosi, C. 2000, A&AS, 141, 371

Gómez-González, V. M. A., Mayya, Y. D., & Rosa-González, D. 2016, MNRAS, 460, 155

González-Lópezlira, R. A., Lomelí-Núñez, L., Álamo-Martínez, K., et al. 2017, ApJ, 835, 184

Harris, G. L. H., & Harris, W. E. 2011, MNRAS, 410, 2347

Harris, G. L. H., Poole, G. B., & Harris, W. E. 2014, MNRAS, 438, 2117

Harris, W. E. 1996, AJ, 112, 1487

Harris, W. E., Blakeslee, J. P., & Harris, G. L. H. 2017, ApJ, 836, 67

Harris, W. E., Harris, G. L. H., & Alessi, M. 2013, ApJ, 772, 82

Harrison, C. M., Johnson, H. L., Swinbank, A. M., et al. 2017, MNRAS, 467, 1965

Heald, G., Józsa, G., Serra, P., et al. 2011, A&A, 526, A118

Humphreys, E. M. L., Reid, M. J., Moran, J. M., Greenhill, L. J., & Argon, A. L. 2013, ApJ, 775, 13

Kissler-Patig, M., Ashman, K. M., Zepf, S. E., & Freeman, K. C. 1999, AJ, 118, 197

Kron, R. G. 1980, ApJS, 43, 305

Kruijssen, J. M. D. 2015, MNRAS, 454, 1658

Kurtz, M. J., & Mink, D. J. 1998, PASP, 110, 934

Larsen, S. S. 1999, A&AS, 139, 393

Läsker, R., Greene, J. E., Seth, A., et al. 2016, ApJ, 825, 3

Lee, M. G., Hwang, H. S., Kim, S. C., et al. 2008, ApJ, 674, 886

Lupton, R., & Monger, P. 1991, SuperMongo (Princeton, NJ: Princeton Univ. Press)

Lupton, R. H. 1989, AJ, 97, 1350

Muñoz, R. P., Puzia, T. H., Lançon, A., et al. 2014, ApJS, 210, 4

Nantais, J. B., & Huchra, J. P. 2010, AJ, 139, 2620

Patrício, V., Richard, J., Carton, D., et al. 2018, MNRAS, 477, 18

Pawlowski, M. S., Pflamm-Altenburg, J., & Kroupa, P. 2012, MNRAS, 423, 1109

Peng, C. Y., Ho, L. C., Impey, C. D., & Rix, H.-W. 2010, AJ, 139, 2097

Peng, E. W., Jordán, A., Côté, P., et al. 2008, ApJ, 681, 197

Perrett, K. M., Bridges, T. J., Hanes, D. A., et al. 2002, AJ, 123, 2490

Powalka, M., Lançon, A., Puzia, T. H., et al. 2016, ApJS, 227, 12

Reid, M. J., Menten, K. M., Brunthaler, A., et al. 2014, ApJ, 783, 130

Rhode, K. L. 2012, AJ, 144, 154

Robin, A., & Creze, M. 1986, A&A, 157, 71

Rodriguez-Gomez, V., Genel, S., Vogelsberger, M., et al. 2015, MNRAS, 449, 49

Sadoun, R., & Colin, J. 2012, MNRAS, 426, L51

Schlafly, E. F., & Finkbeiner, D. P. 2011, ApJ, 737, 103

Spitler, L. R., & Forbes, D. A. 2009, MNRAS, 392, L1

Tacconi, L. J., Neri, R., Genzel, R., et al. 2013, ApJ, 768, 74

Terlouw, J. P., & Vogelaar, M. G. R. 2015, Kapteyn Package v.2.3, (Groningen: Kapteyn Astronomical Institute), http://www.astro.rug.nl/software/kapteyn/

Tody, D. 1986, Proc. SPIE, 627, 733

Tody, D. 1993, in ASP Conf. Ser. 52, Astronomical Data Analysis Software and Systems II, ed. R. J. Hanisch, R. J. V. Brissenden, & J. Barnes (San Francisco, CA: ASP), 173

Turner, O. J., Cirasuolo, M., Harrison, C. M., et al. 2017, MNRAS, 471, 1280

White, R. E., & Shawl, S. J. 1987, ApJ, 317, 246

Wisnioski, E., Förster Schreiber, N. M., Wuyts, S., et al. 2015, ApJ, 799, 209

Wolf, M. J., Drory, N., Gebhardt, K., & Hill, G. J. 2007, ApJ, 655, 179